SCIENTIFIC REPORTS

OPEN

SUBJECT AREAS:
MORPHOGENESIS
MECHANICAL ENGINEERING

Received
28 October 2014

Accepted
6 February 2015

Published
9 March 2015

Correspondence and requests for materials should be addressed to X.Z. (zhaox@mit.edu)

A three-dimensional phase diagram of growth-induced surface instabilities

Qiming Wang[1,2] & Xuanhe Zhao[1,2,3]

[1]Soft Active Materials Laboratory, Department of Mechanical Engineering, Massachusetts Institute of Technology, Cambridge, Massachusetts 02139, USA, [2]Department of Mechanical Engineering and Materials Science, Duke University, Durham, North Carolina 27708, USA, [3]Department of Civil and Environmental Engineering, Massachusetts Institute of Technology, Cambridge, MA 02139, USA.

A variety of fascinating morphological patterns arise on surfaces of growing, developing or aging tissues, organs and microorganism colonies. These patterns can be classified into creases, wrinkles, folds, period-doubles, ridges and delaminated-buckles according to their distinctive topographical characteristics. One universal mechanism for the pattern formation has been long believed to be the mismatch strains between biological layers with different expanding or shrinking rates, which induce mechanical instabilities. However, a general model that accounts for the formation and evolution of these various surface-instability patterns still does not exist. Here, we take biological structures at their current states as thermodynamic systems, treat each instability pattern as a thermodynamic phase, and construct a unified phase diagram that can quantitatively predict various types of growth-induced surface instabilities. We further validate the phase diagram with our experiments on surface instabilities induced by mismatch strains as well as the reported data on growth-induced instabilities in various biological systems. The predicted wavelengths and amplitudes of various instability patterns match well with our experimental data. It is expected that the unified phase diagram will not only advance the understanding of biological morphogenesis, but also significantly facilitate the design of new materials and structures by rationally harnessing surface instabilities.

Numerous intriguing morphologies and phenomena on surfaces of growing animals, plants and microorganism colonies have fascinated artists and scientists for decades[1,2]. Abundant examples (Fig. 1A) can be found in various types of living creatures across multiple size scales, such as wrinkles on skins of mammalians, plants and fruits[3–8], undulations in developing biofilms[9–11], grooves on the cerebral cortex[12–15], mucosal villi and folds of airways, esophagi and guts[16–22], buckled tumor surfaces[23,24], epithelial cell delamination due to tissue crowding[25,26], and crumpled membranes of blood cells[27]. Although these biological patterns may be results of complex genetic, biological and biochemical processes, recent studies have suggested that growth-induced mechanical forces regulate the formation and evolution of biological patterns[2,16,18,28–30]. Biological structures usually consist of multiple layers with strikingly different biochemical compositions and mechanical properties; for example, epidermis on the dermis or hypodermis of mammalian skins[3–5], the epidermis on the ground tissue of plant skins[6–8], biofilms on culture gels[9–11], the grey matter on the white matter of cerebral cortexes[12,13], the mucosa on the muscle layer of airways, esophagi and guts[16–22], outer proliferative cells on the inner necrotic core of a tumor[23], epithelial cell monolayer on the underlying tissue[25,26], membranes on the cytoskeleton of blood cells[27]. During growth, development or aging, different layers of biological structures usually have different expanding or shrinking rates, thus resulting in mismatch strains between the biological layers. The surface topographical patterns have long been believed to be results of mismatch-induced compressive strains in the skin layers which have higher growth rates or lower shrinkage rates than the underlying biological layers[14–16,18,31]. Once the mismatch compressive strain rises to critical values, the initially flat surface of the film becomes unstable and bifurcate into different types of corrugated patterns (Fig. 1B), including (i) *wrinkle* — the film undulates sinusoidally but remains locally smooth (e.g., the pumpkin skin in Figs 1Ai and 1Bi)[6], (ii) *crease* — the surface of the film folds into dispersed regions of self-contacts with sharp tips (e.g., the cerebral cortex in Figs 1Aii and 1Bii)[12,32], and (iii) *delaminated-buckle* — the film delaminates from the substrate to form buckled regions (e.g., the biofilm in Figs 1Aiii and 1Biii)[10]. As the mismatch strain further increases, the wrinkles may further bifurcate into more complicated surface patterns, including (iv) *fold* – some valleys of the wrinkle fold into self-contacts with sharp tips (e.g., the dog skin in Figs 1Aiv and 1Biv)[33], (v) *period-double* — the sinusoidal wrinkle transits into a pattern with twice of the wavelength (Fig. 1Bv), and (vi) *ridge* — the wrinkle drastically increases its

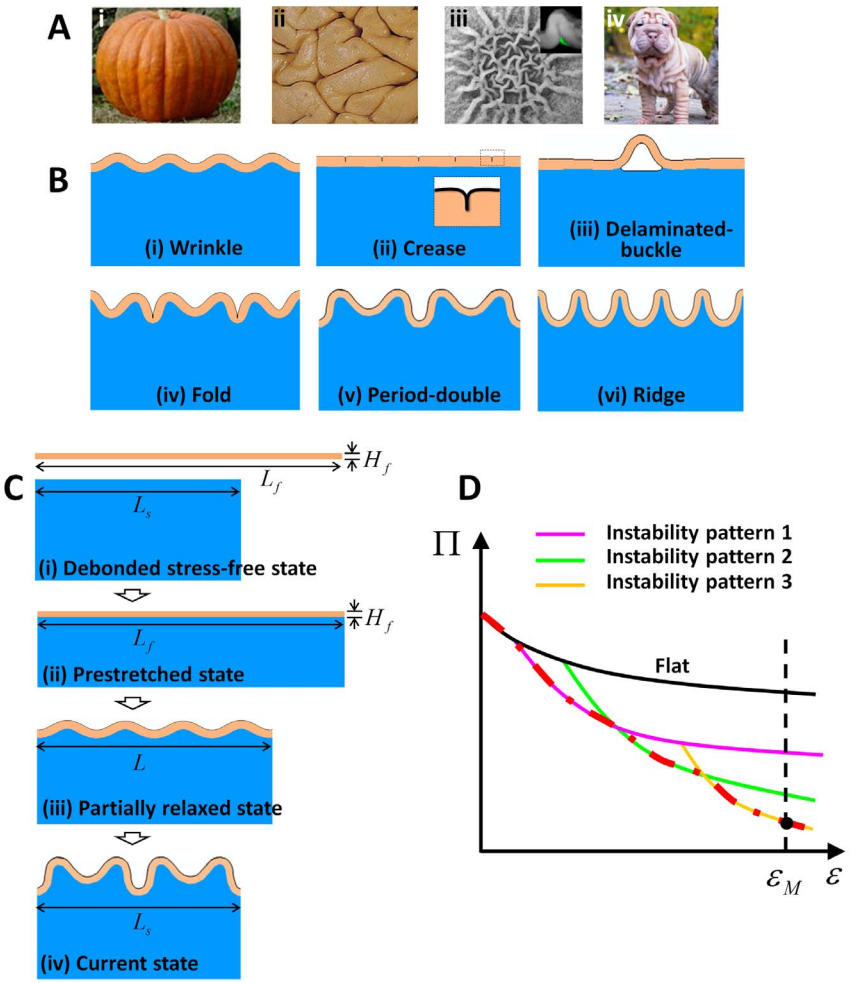

Figure 1 | Illustrations of examples, schematics and potential energies of various growth-induced surface instabilities. (A) Examples of growth-induced surface instabilities on (i) the pumpkin skin, (ii) the cerebral cortex, (iii) the biofilm and (iv) the dog skin. (B) Schematics of growth-induced surface instabilities: (i) wrinkle, (ii) crease, (iii) delaminated-buckle, (iv) fold, (v) period-double and (vi) ridge. (C) One example pathway to induce the mismatch strain in the film-substrate structure: (i) The film and substrate is first assumed to be detached from each other to form a stress-free state; (ii) the detached stress-free substrate is then pre-stretched by a ratio of L_f/L_s and adhered to the film; (iii) relaxed to length L; and (iv) eventually relaxed to length L_s at the current state. Other pathways to induce mismatch strains are illustrated in Supplementary Figs S5 and S7. (D) Evolution of potential energy of the film-substrate structure with increasing mismatch strain following the pathway in (C). The red dash line denotes the surface patterns with the minimum potential energy. The potential energy of the film-substrate structure with mismatch strain ε_M is denoted by the black solid circle. Image (Ai) is reprinted with permission from Yin, et al., Proc. Natl. Acad. Sci. U.S.A., 105, 49 (2008). Copyright 2008, National Academy of Sciences, USA. Image (Aii) is reprinted from Bradbury, PLOS Biol., 3, 3 (2005) under Open-Access License. Image (Aiii) is reprinted with permission from Asally, et al., Proc. Natl. Acad. Sci. U.S.A., 109, 46 (2012). Copyright 2012, National Academy of Sciences, USA. Image (Aiv) is reprinted with permission from Alison Ruhe.

amplitude but decreases its wavelength, forming a high-aspect-ratio pattern that ceases to follow sinusoidal shape (Fig. 1Bvi). These instability patterns with distinctive topographical characteristics have been only studied and identified separately in different biological systems under varied physical and biological conditions[6,10,16,18,25]. However, a general model that can quantitatively predict the formation and evolution of various types of surface-instability patterns still does not exist; primarily because existing theories such as linear stability analysis cannot systematically analyze all modes of instabilities[12], and existing experiments did not systematically vary the mechanical properties of film-substrate systems.

Here, we take biological film-substrate structures at their current states as thermodynamic systems, and regard each mode of surface-instability pattern as a thermodynamic phase. By systematically varying mechanical properties of the structure including moduli, adhesion energy and mismatch strain of the film and substrate, we calculate the initiation and evolution of various modes of growth-induced surface instabilities. We then compare potential energies of different instability patterns, and construct a quantitative phase diagram that accounts for all instability patterns discussed above, by assuming the current pattern seeks the lowest potential energy among all possible configurations. To validate the phase diagram, we impose different mismatch strains in polymeric film-substrate structures with systematically varied rigidity and adhesion energy to induce various modes of instability patterns. The resultant patterns indeed follow the phase diagram quantitatively. We further find that the phase diagram agrees well with reported data on growth-induced surface instabilities from a number of previous studies. It is expected that the phase diagram will not only advance the understanding of biological morphogenesis, but also significantly facilitate the design of new structures with innovative surfaces or interfaces for disease therapy[22,24], active cell culture[34], biofouling management[35], tunable superhydrophobicity[36] and flexible electronics[37,38].

Results

A three-dimensional phase diagram. While the development of instability patterns in biological structures may involve compli-

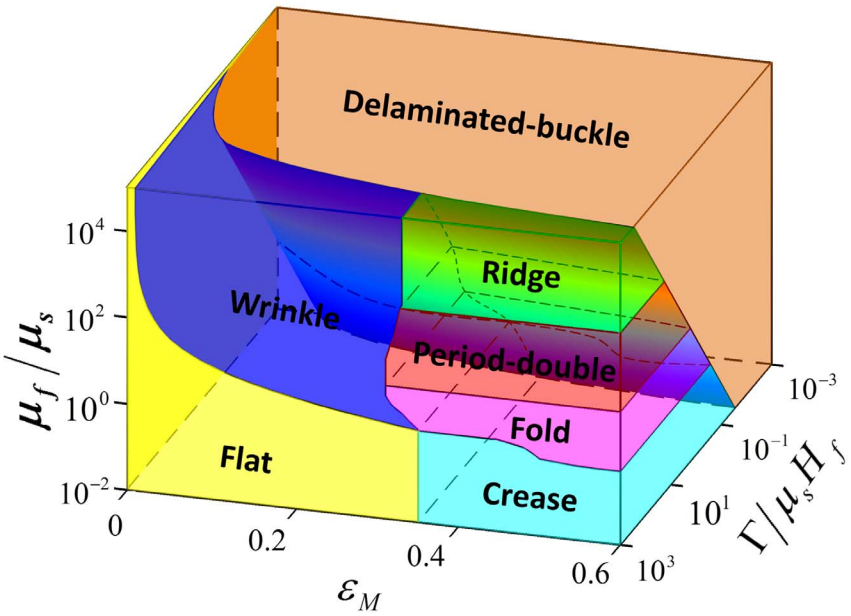

Figure 2 | A calculated three-dimensional phase diagram of various surface instability patterns induced by mismatch strains. The instability pattern is determined by three non-dimensional parameters: mismatch strain ε_M, modulus ratio μ_f/μ_s and normalized adhesion energy $\Gamma/(\mu_s H_f)$.

cated biological processes, determining the instability patterns at current states can be solved as mechanics problems[2,16,18,28–30]. To focus on essential physical features, we simplify the layered biological structures at the current states as a homogeneous film adhered on a homogeneous underlying substrate, both undergoing plane-strain deformation (Fig. 1C). To account for large deformation, both the film and the substrate are taken as incompressible neo-Hookean materials with shear modulus μ_f and μ_s, respectively. If the film and the substrate at the current state are detached from each other, they will have lengths L_f and L_s and thicknesses H_f and H_s, respectively (Fig. 1Ci). We define the mismatch strain between the film and the substrate at current state as $\varepsilon_M = (L_f - L_s)/L_f$. Since film thickness H_f is much smaller than all the other dimensions (i.e., L_f, L_s and H_s) in the system, it is the only relevant length scale for analyzing the instability patterns. We further define the adhesion energy between the film and the substrate, Γ, as the work required to detach the film from a unit area of the substrate in the stress-free state.

Within the time scale of determining instability patterns, we take the film-substrate structure as a thermodynamic system, and assume the current surface-instability pattern always seeks the lowest potential energy among all possible configurations (Fig. 1D), *i.e.*, following the Maxwell stability criterion[39–42]. The potential energy per unit width of the film-substrate system under plane-strain deformation can be expressed as[39]

$$\Pi = U_f + U_s + \Gamma D \tag{1}$$

where U_f and U_s are strain energies per unit width of the film and substrate, respectively, and D is the current delaminated length of the substrate measured in the stress-free state (Fig. 1Ci). This simplified model involves five physical parameters that determine the instability patterns: μ_f, μ_s, H_f, Γ and ε_M. By dimensional argument, they can be normalized into three dimensionless parameters: modulus ratio μ_f/μ_s, normalized adhesion energy $\Gamma/(\mu_s H_f)$ and mismatch strain ε_M. The types of instability patterns will be solely determined by the three dimensionless parameters, and therefore governed by a three-dimensional phase diagram. It should be noted that biological structures can take different paths to induce mismatch strains such as expansion of films or shrink of substrates (see *e.g.*, Supplementary Figs S5 and S7); however, structures with the same set of μ_f/μ_s, $\Gamma/(\mu_s H_f)$ and ε_M should reach the same type of instability pattern at the current state, given the Maxwell stability criterion is followed.

Next, we discuss the process to quantitatively construct the phase diagram. A plane-strain finite element model is developed to calculate the formation of instability patterns (Methods and SI). To induce mismatch strains in the model, we assume the detached stress-free substrate in Fig. 1Ci is pre-stretched by a ratio of L_f/L_s, adhered to the film (Fig. 1Cii), and then relaxed to length L (Fig. 1Ciii), during which all deformation occurs in plane-strain condition. The overall compressive strain in the film is defined as $\varepsilon = (L_f - L)/L_f$ (Fig. 1Ciii). As ε increases to critical values, patterns of surface instabilities can initiate and transit into others (Fig. 1D). Force perturbations and mesh defects have been introduced into the model as fluctuations to facilitate the system to seek minimum-potential energy states (Fig. 1D). When the substrate is fully relaxed (*i.e.*, $L = L_s$ and $\varepsilon = \varepsilon_M$, shown as the black solid circle on Fig. 1D), the resultant pattern is the instability pattern of the film-substrate system with mismatch strain ε_M, which represents a point of one phase in the phase diagram (Fig. 2). The boundaries between regions of different phases give the phase boundaries on the phase diagram. We can also determine the phase boundaries by comparing the potential energies of different patterns with the same set of μ_f/μ_s, $\Gamma/(\mu_s H_f)$ and ε_M[39,43,44], i.e.,

$$\Pi_i = \Pi_j \tag{2}$$

where Π_i and Π_j are the potential energies of two different patterns on film-substrate models with the same properties and dimensions (Fig. 1D). Following this method, we categorize all modes of surface instabilities patterns discussed above into a three-dimensional phase diagram with quantitatively determined phase boundaries (Fig. 2).

To understand the phase diagram, we first consider the scenario in which the adhesion between the film and the substrate is so strong that the film does not delaminate from the substrate (*i.e.*, $D = 0$). The instability patterns are thus governed only by μ_f/μ_s and ε_M, giving a two-dimensional phase diagram (*i.e.*, $\Gamma/(\mu_s H_f) \to \infty$ on Figs 2 and 3A). When the mismatch strain ε_M is sufficiently low, the flat film-substrate structure has lower potential energy than any instability pattern. As the mismatch strain increases to critical values, the flat state will transit into either wrinkled or creased state, depending on the modulus ratio. When $\mu_f/\mu_s < 1.3$ (*i.e.*, relatively compliant film), the film tends to fold against itself without deforming the substrate to

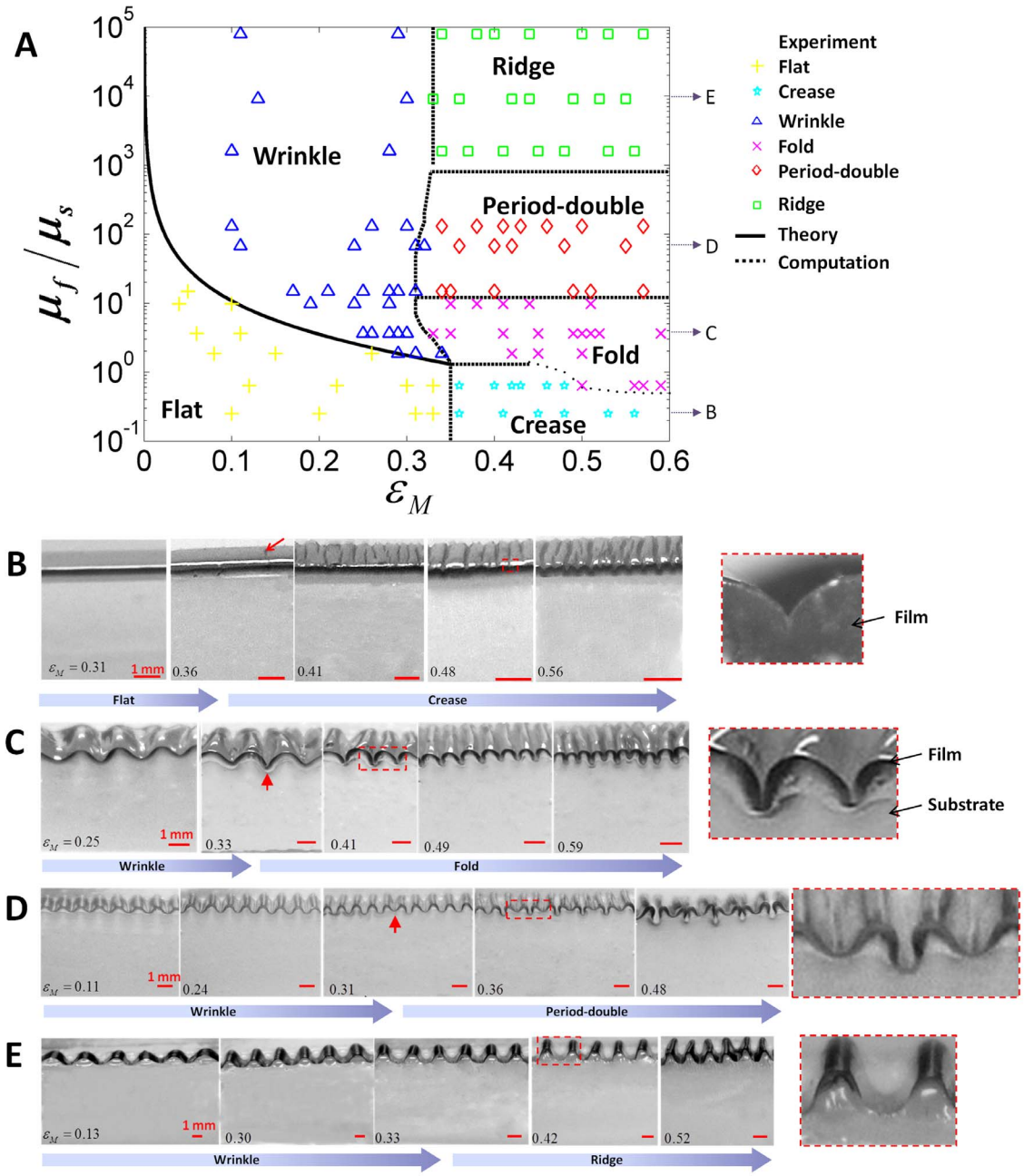

Figure 3 | Experimental validation of the phase diagram for instability patterns in film-substrate structures with high adhesion energies. (A) Comparison between experimental data and the phase diagram of surface instability patterns without delamination. Experimental images to show the formation of (B) creases, (C) wrinkles and folds, (D) wrinkles and period-doubles, and (E) wrinkles and ridges in film-substrate structures with different modulus ratios and mismatch strains. The film-substrate modulus ratios are (B) 0.3, (C) 3.64, (D) 67.24 and (E) 9110, respectively.

minimize the potential energy of the system. The phase boundary between the flat and creased states, which is calculated by setting $\Pi_{flat} = \Pi_{crease}$[12,43], is a vertical line on Figs 2 and 3A,

$$\varepsilon^C_{crease} = 0.35 \ for \ \mu_f/\mu_s < 1.3 \tag{3}$$

where ε^C_{crease} is the critical mismatch strain, at which the structure transits from flat to creased state. It is noted that, for $0.5 < \mu_f/\mu_s < 1.3$, the creases may further develop into folds under larger mismatch strains, *i.e.*, $\varepsilon_M > 0.45$ (Supplementary Fig. S1).

On the other hand, when $\mu_f/\mu_s > 1.3$ (*i.e.*, relatively stiff film), the film tends to undulate together with the substrate to minimize the potential energy of the system. The phase boundary between the flat and creased states, which is calculated by setting $\Pi_{flat} = \Pi_{wrinkle}$ (See SI and Supplementary Fig. S2), can be approximated as a curve on Figs 2 and 3A,

$$\varepsilon^C_{wrinkle} \approx \begin{cases} 0.41\left(\dfrac{\mu_f}{\mu_s}\right)^{-0.59} & for \quad 1.3 \le \dfrac{\mu_f}{\mu_s} \le 16 \\ 0.50\left(\dfrac{\mu_f}{\mu_s}\right)^{-0.66} & for \quad \dfrac{\mu_f}{\mu_s} > 16 \end{cases} \tag{4}$$

where $\varepsilon^C_{wrinkle}$ is the critical mismatch strain, at which the structure transits from flat to wrinkle state. Notably, the triple point between flat, creased and wrinkled states in a film-substrate structure with mismatch strain is at $\varepsilon_M = 0.35$ and $\mu_f/\mu_s = 1.3$.

As the mismatch strain further increases, the wrinkled film-substrate structure can further bifurcate into more complicated pat-

terns including fold, period-double and ridge, depending on the modulus ratio μ_f/μ_s. Qualitatively, the pattern of fold develops at a lower range of μ_f/μ_s (*i.e.*, relatively compliant films) than period double and ridge, because the fold requires large deformation and self-contact of films. Quantitatively, the calculated phase boundaries between fold, period-double and ridge are approximately horizontal lines at $\mu_f/\mu_s \approx 12$ and $\mu_f/\mu_s \approx 800$, respectively, in the region of $0.3 < \varepsilon_M < 0.6$ (Figs 2 and 3A). In addition, the calculated phase boundary between wrinkle and fold is in the region of $1.3 < \mu_f/\mu_s < 12$ and $0.3 < \varepsilon_M < 0.35$ (Figs 2 and 3A, Supplementary Fig. S3); between wrinkle and period double in the region of $12 < \mu_f/\mu_s \leq 800$ and $0.3 < \varepsilon_M < 0.32$ (Figs 2 and 3A, Supplementary Figs S4 and S5); and between wrinkle and ridge states in the region of $800 < \mu_f/\mu_s < 10^6$ and $\varepsilon_M \approx 0.33$ (Figs 2 and 3A, Supplementary Figs S6 and S7). If the mismatch strain increases beyond 0.6, more complicated patterns will develop, such as period triple[45,46], period quadruples[45], and co-existence of fold, period double and ridge, which will be not be covered in the current paper. It should be noted, since the Maxwell stability criterion is followed here, the formation of these instability patterns is independent on the processes of inducing mismatch strains. Our finite-element calculations indeed give the same instability patterns, while following different pathways to induce the mismatch strains, such as substrate pre-stretching and relaxing, film swelling and substrate shrinking (Fig. 1C, Supplementary Figs S5 and S7).

Next, we discuss the scenario in which the adhesion between the film and substrate is relatively weak (i.e., relatively low $\Gamma/(\mu_s H_f)$) and the film debonds from the substrate to form delaminated-buckles (i.e., $D > 0$). To calculate the potential energy of a delaminated-buckled pattern Π_{buckle}, we first prescribe various pairs of delaminated length D and delaminated-buckle wavelength λ in the finite-element model (See Supplementary Figs S8A, S9A and S10A). Minimization of the potential energy of the structure requires[47]

$$\frac{\partial(\Pi_{buckle}/\lambda)}{\partial D} = 0 \tag{5}$$

$$\frac{\partial(\Pi_{buckle}/\lambda)}{\partial \lambda} = 0 \tag{6}$$

By solving Eqs. 5 and 6, we can obtain a set of D, λ and Π_{buckle} for the film-substrate structure, which is assumed to be in the delaminated-buckled state (Supplementary Figs S8B, S9B and S10B). To calculate the phase boundary between the delaminated-buckle and other states, we set $\Pi_{buckle} = \Pi_{ud}$ for two models with the same properties and dimensions, where Π_{ud} represents the potential energy of an un-delaminated state. For fixed values of μ_f/μ_s and ε_M, it is evident that Π_{buckle} is a monotonically increasing function of $\Gamma/(\mu_s H_f)$ but Π_{ud} is a constant (Supplementary Figs S8C, S9C, and S10C). Therefore, the critical value of $\Gamma/(\mu_s H_f)$ on the phase boundary between the delaminated-buckled state and un-delaminated states is determined by the intersections of the two curves of Π_{buckle} and Π_{ud} (Supplementary Fig. S11).

Overall, the three-dimensional phase diagram for growth-induced surface instabilities in film-substrate structures can be understood as follows (Fig. 2). As the mismatch strains in film-substrate structures reach critical values, the initially flat structures can transit into various types of surface instability patterns. If the normalized adhesion energies between the films and substrates are sufficiently high, the preferable patterns are crease and fold for structures with relatively compliant films, but wrinkle, period double and ridge for structures with relatively stiff films. As the normalized adhesion energy decreases to critical values, the un-delaminated patterns transit into the delaminated-buckle patterns.

Wavelengths and amplitudes of growth-induced surface instabilities. We next study the wavelengths and amplitudes of instability patterns on the phase diagram (Fig. 2). For a film-substrate system with $\mu_f/\mu_s < 1.3$, a mismatch strain above 0.35 induces nucleation of scattered creases on the surface of the film; further increasing ε_M leads to a pattern of creases with a wavelength λ_{crease} (Supplementary Fig. S13). The wavelength of the crease pattern approximately follows a linear relation with ε_M as[48]

$$\lambda_{crease}/H_f = 3.5(1-\varepsilon_M) \tag{7}$$

which matches consistently with the current experimental data and the previous study on crease pattern in materials under compression[48] (Supplementary Fig. S13).

If the modulus ratio of the system μ_f/μ_s is above 1.3, the initially flat surface first bifurcates into the wrinkle phase. The wavelength of the wrinkles at initiation (i.e., just transited from flat state) can be calculated by linear stability analysis and expressed as a function of μ_f/μ_s(see SI and Supplementary Fig. S2D)[49]. For large modulus ratios (i.e., $\mu_f/\mu_s > 10^3$), the wavelength of wrinkles at initiation can be approximated as[50]

$$\lambda^C_{wrinkle}/H_f = 2\pi\left(\mu_f/3\mu_s\right)^{1/3} \tag{8}$$

Further increasing the mismatch strain will decrease the wavelengths of the wrinkles. We adopt a modified accordion model to calculate the wavelength of wrinkles with increased mismatch strain. Without loss of generality, let's consider a case that the mismatch strain is induced by the shrinkage of the substrate and the length of the film maintains constant during the process, as illustrate in Supplementary Fig. S14. At a critical mismatch strain, wrinkles with initial wavelength sets in the film-substrate structure. The modified accordion model assumes that the number of undulations in the wrinkles does not change as the substrate further shrinks to increase the mismatch strain above the critical mismatch strain. Therefore, the wavelength of the wrinkles varies according to the mismatch strains at wrinkle initiation and current state, as[37,38,45]

$$\frac{\lambda_{wrinkle}}{\lambda^C_{wrinkle}} \approx \frac{1-\varepsilon_M}{1-\varepsilon^C_{wrinkle}} \tag{9}$$

where $\varepsilon^C_{wrinkle}$ is the critical mismatch strain for wrinkle initiation, given by Eq. 4. The modified accordion model further assumes that the number of undulations in the patterns still maintain the same when the wrinkles transit into folds, period doubles and ridges due to further shrinkage of the substrate. Therefore, we can calculate the wavelengths of folds, period doubles and ridges under various mismatch strains, respectively, as

$$\frac{\lambda_{fold}}{\lambda^C_{wrinkle}} \approx \frac{1-\varepsilon_M}{1-\varepsilon^C_{wrinkle}} \tag{10}$$

$$\frac{\lambda_{period-double}}{\lambda^C_{wrinkle}} \approx \frac{2(1-\varepsilon_M)}{1-\varepsilon^C_{wrinkle}} \tag{11}$$

$$\frac{\lambda_{ridge}}{\lambda^C_{wrinkle}} \approx \frac{1-\varepsilon_M}{1-\varepsilon^C_{wrinkle}} \tag{12}$$

It is noted that the period-double has a wavelength twice of the corresponding wrinkles, as given in Eq. 11.

Once the wavelengths of wrinkles are obtained from Eq. 9, we can further calculate the amplitude of wrinkles by approximating the arc-length of wrinkles at various mismatch strains to be equal to the wavelength of wrinkles at initiation (See Supplementary Fig. S14)[37,38], i.e.,

$$\int_0^{\lambda_{wrinkle}} \sqrt{1+\left[\left(A_{wrinkle}\sin\frac{2\pi x}{\lambda_{wrinkle}}\right)'\right]^2}\,dx \approx \lambda^C_{wrinkle} \tag{13}$$

where $()'$ is differential operation for x.

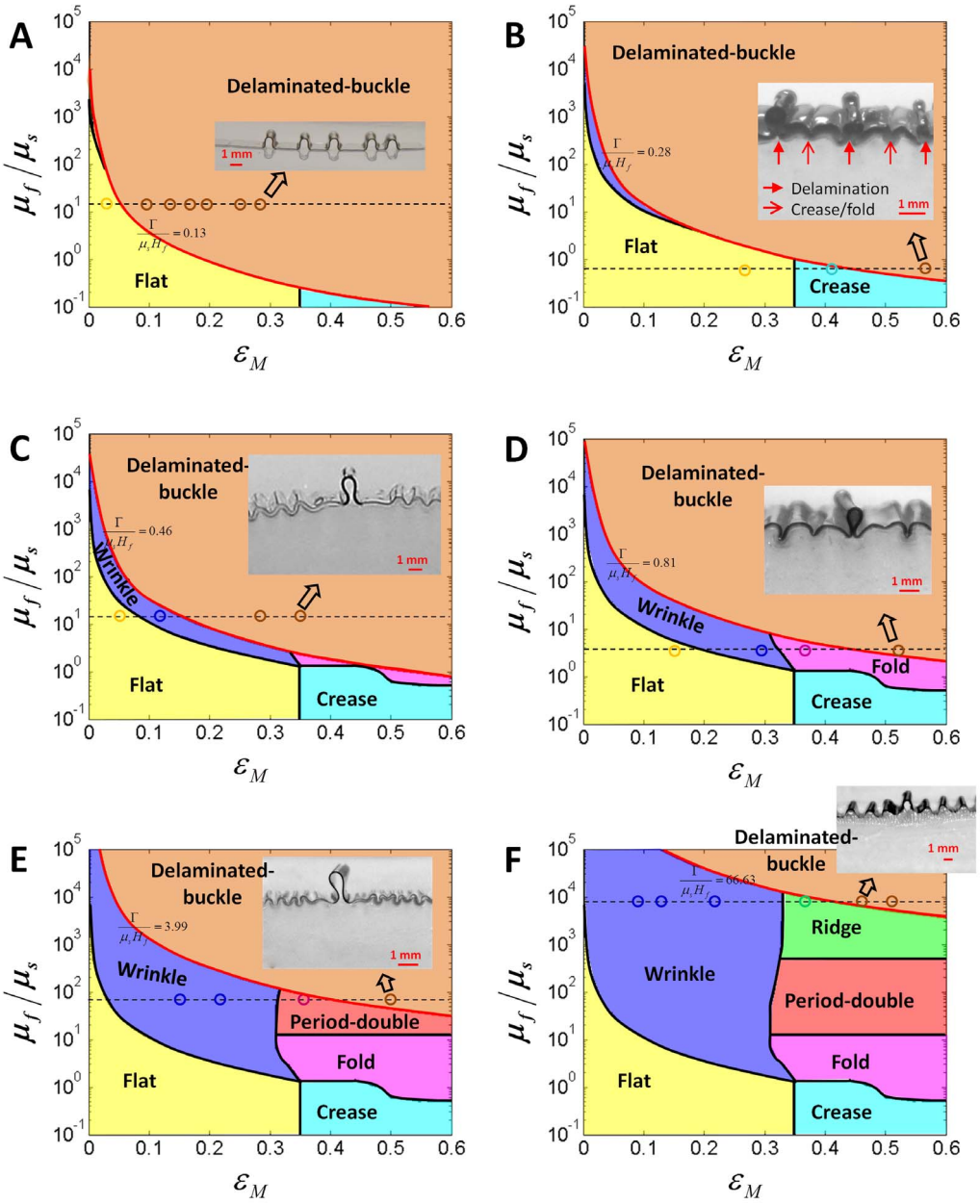

Figure 4 | Experimental validation of the phase diagram for instability patterns in film-substrate structures with moderate adhesion energies. Comparison between experimental data and the phase diagrams of surface instability patterns with delamination: (A) flat to delaminated-buckle, (B) crease to delaminated-buckle, (C) wrinkle to delaminated-buckle, (D) fold to delaminated-buckle, (E) period-double to delaminated-buckle, and (F) ridge to delaminated-buckle. The circle markers with different colors in each phase domain represent the observed instability patterns. The inset images in each phase diagram represent the corresponding delaminated-buckle patterns. The two-dimensional phase diagrams are achieved by sectioning the three-dimensional phase diagram at the normalized adhesion energies $\Gamma/(\mu_s H_f)$ equal to (A) 0.13, (B) 0.28, (C) 0.46, (D) 0.81, (E) 3.99 and (F) 66.63, respectively.

Validation of the theoretical models with experiments. We next verify the 3D phase diagram by comparing with experimental results on polymeric film-substrate structures with mismatch strains. We induce the mismatch strain in the film-substrate structure by uniaxially pre-stretching an elastomer substrate, adhering a polymer film on the substrate, and then relaxing the substrate to the original length (see Methods and Fig. 1C). While the shear modulus of the substrate is fixed to be 10.4 *kPa*, the shear modulus of the film is varied from ~3 *kPa* to ~0.8 *GPa*, giving modulus ratio μ_f/μ_s from ~0.3 to ~8×10^4. The adhesion energy between the film and substrate is controlled to vary from 10^{-2} Jm^{-2} to 10^3 Jm^{-2} by baking the film-substrate structures at different temperatures (see Methods and Supplementary Fig. S12)[39]. In order to avoid the film-substrate delamination, a very high adhesion energy (*i.e.*, $\Gamma > 10^3$ Jm^{-2} and $\Gamma/(\mu_s H_f) > 10^3$) is achieved by smearing a thin adhesive layer between the film and substrate[47,48,51]. Since the adhesive layer is much thinner than the film and its modulus approximates that of the substrate, the adhesive layer does not affect the instability patterns[39].

We first discuss the five modes of patterns observed in the film-substrate structures with strong adhesion that prevents delamination: (i) If the film is more compliant than the substrate, for example $\mu_f/\mu_s = 0.3$ or 0.64, the structure maintains flat under relatively low mismatch strain. When ε_M reaches ~0.36 (for $\mu_f/\mu_s = 0.3$ and 0.64), the initially flat surface suddenly forms discrete creases as indicated by arrows in Fig. 3B, which then evolve into periodically distributed creases with the rise of ε_M[12,43]. (ii) When the modulus ratio increases

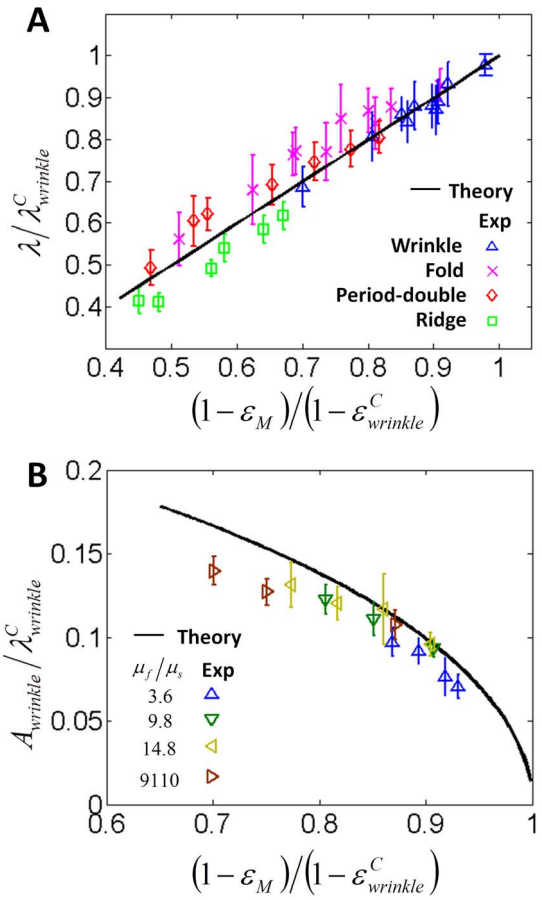

Figure 5 | Wavelengths and amplitudes of wrinkles and other instability phases. (A) Wavelengths of wrinkles, folds and ridges, and half wavelength of period-doubles varied with the mismatch strains. (B) Amplitudes of wrinkles varied with the mismatch strains and the modulus ratios.

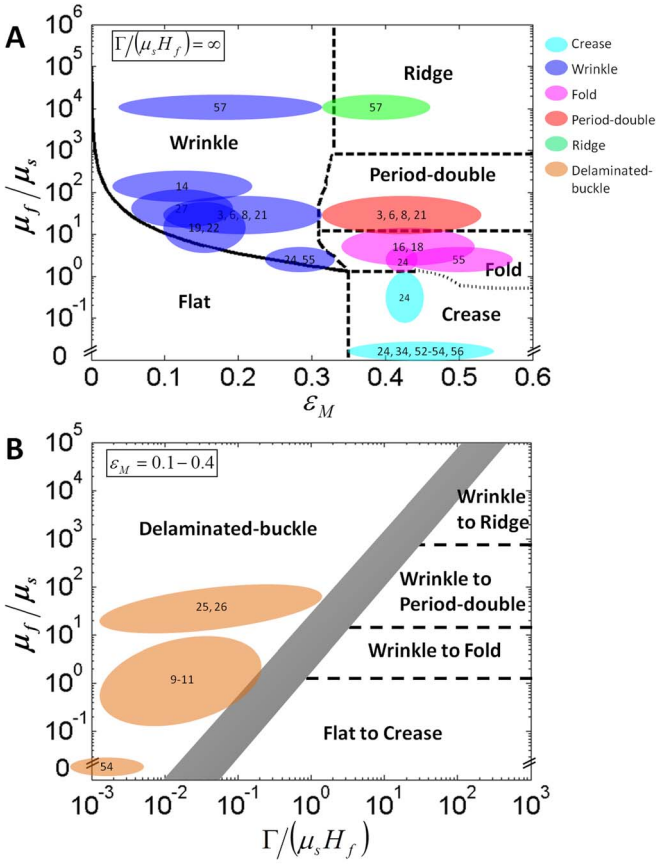

Figure 6 | Validation of the phase diagram with reported experimental data. The previous studies on growth/swelling induced surface instabilities for film-substrate structures with (A) high adhesion energies that prevent delamination and (B) moderate adhesion energies that permit delamination. The numbers in the colored domains denote the reference number. The two-dimensional phase diagram in (B) is achieved by stacking the three-dimensional phase diagram in the region of $\varepsilon_M = 0.1 - 0.4$.

to a range of $\mu_f/\mu_s = 1.84 - 7.94 \times 10^4$, the initially flat structure first forms wrinkles under moderate mismatch strains (Figs. 3C–3E). As the mismatch strains further increase to critical values, the wrinkles can bifurcate into folds, period doubles or ridges, depending on the modulus ratio. (iii) If the film is slightly stiffer than the substrate with μ_f/μ_s = 1.86, 3.64 or 9.79, the wrinkled surface folds against itself to form creases at some valleys once ε_M reaches ~0.33 (Fig. 3C). With further increase of mismatch strain, all valleys sequentially collapse into folds and further penetrate into the substrate (e.g., ε_M = 0.59 in Fig. 3C). (iv) When the modulus ratio is further increased to a higher range, with μ_f/μ_s = 14.77, 67.24 or 130.74, the wrinkles transit into period-doubles at $\varepsilon_M \approx 0.32$, by growing the amplitude of one wrinkle at the expense of its neighbors (Fig. 3D). With further increasing ε_M, the crests of period doubles may contact each other to form channels in the valleys (see ε_M = 0.48 in Fig. 3D). (v) If the film is much stiffer than the substrate, for example $\mu_f/\mu_s = 1.59 \times 10^3, 9.11 \times 10^3$ or 7.94×10^4, the wrinkles bifurcate into ridge at $\varepsilon_M \approx$ 0.33 (Figs. 3A and 3E). From the comparisons in Fig 3A, it can be seen the observed patterns of creases, wrinkles, folds, period doubles and ridges follow consistently with the prediction of the phase diagram.

Next, we discuss the observed patterns in film-substrate structures with moderate adhesion energies, which allow delamination between films and substrates. To compare the experimental observations with the calculated phase diagram, we section the three-dimensional phase diagram at various values of normalized adhesion energy, *i.e.*, $\Gamma/(\mu_s H_f)$ = 0.13, 0.28, 0.46, 0.81, 3.99 and 66.63 (Fig. 4). The phase boundaries between delaminated-buckle and other patterns are highlighted as red curves in these sections. From Fig. 4, it can be seen that the observed transitions of phases with the increase of ε_M indeed follow the calculated phase diagram, for various values of $\Gamma/(\mu_s H_f)$ and μ_f/μ_s. In particular, the delaminated-buckle can coexist with other instability patterns, and the phase boundaries between delaminated-buckle and other patterns can consistently predict whether delamination occurs in the film-substrate structures.

Finally, the wavelengths and amplitudes of the instability patterns are also validated by our experimental results. As shown in Fig. 5A, the experimentally observed wavelengths of the wrinkles, folds, period-doubles and ridges at varied mismatch strains match consistently with the predictions from Eqs. 9–12. In addition, combining Eq. 13 and $\lambda^C_{wrinkle}$ in Eq. 8, we compute the amplitude of the wrinkle for various μ_f/μ_s and ε_M in Fig. 5B. The calculated amplitudes of wrinkles match well with the experimental data for low modulus ratios, and the discrepancies for high modulus ratios are within 10% (Fig. 5B).

Discussion

The three-dimensional phase diagram is not only validated by our experimental results, but also by reported data on surface instabilities in various biological and biomimetic film-substrate structures. Figure 6 summaries the growth or swelling induced surface instabilities from a number of biological and biomimetic film-substrate systems, including animal tissue growth[14,16,18,21,22], epithelial monolayer growth[19,25,26], blood cell growth[27], fruit growth or shrinkage[3,6,8], biofilm growth[9–11], and swelling of biomimetic hydrogels and elastomers[24,34,52–57]. The reported or estimated film-substrate modulus

Table 1 | Reported and estimated parameters of growth/swelling film-substrate systems with various surface instabilities in published studies

Reference	System	Instability type	ε_M	μ_f/μ_s	$\Gamma/(\mu_s H_f)$
16,18	tissue	fold	$0.29-0.4$	$1.5-15$	$>10^3$
14	tissue	wrinkle	$0.05-0.18$	$100-300$	$>10^3$
22	tissue	wrinkle	$0.1-0.15$	$5-50$	$>10^3$
21	tissue	wrinkle, period-double	$0.05-0.45$	$10-100$	$>10^3$
19	epithelia	wrinkle	$0.05-0.2$	~ 25	$>10^3$
25,26	epithelia	delaminated-buckle	$0.1-0.22$	$1-100$	$10^{-3}-1$
27	blood cell	wrinkle	$0.05-0.2$	$50-100$	$>10^3$
9–11	biofilm	delaminated-buckle	$0-0.4$	$0.1-10$	$10^{-3}-0.2$
3,6,8	fruit	wrinkle, period-double	$0.1-0.4$	$10-100$	$>10^3$
34,52,53,56	hydrogel	crease	$0.32-0.5$	$<10^{-3}$	$>10^3$
24	hydrogel	crease, wrinkle, fold	$0.25-0.45$	$1-20$	$>10^3$
55	hydrogel	wrinkle, fold	$0.3-0.55$	~ 25	$>10^3$
54	Sylgard	crease, delaminated-buckle	$0.3-0.51$	$<10^{-3}$	$5\times10^{-5}-5\times10^{-3}$
57	Sylgard	wrinkle, ridge	$0.05-0.45$	$\sim 10^4$	$>10^3$

ratios, adhesion energies and mismatch strains are summarized in Table 1 (see details in SI).

From Fig. 6, it can be seen the reported surface instability patterns indeed follow the three-dimensional phase diagram. If the film and the substrate are well bonded (Fig. 6A), swelling gels constrained by a rigid substrate on the bottom with $\mu_f/\mu_s < 10^{-3}$ develop creases on the surfaces[34,52–54,56]. The growing tissues[14,16,18,19,21,22,25,26], tumors[24] and blood cells[27], plant skins[3,6,8], and mammalian skins[3], with μ_f/μ_s in the range of 10^0–10^4, generally develop wrinkles in the systems with small mismatch strains, *i.e.*, $\varepsilon_M = 0.05-0.25$; the wrinkles may further bifurcate into folds in the growing tissues[14,16,18,22] with larger mismatch strains ($\varepsilon_M > 0.3$), or transit into period-double in the mucosal guts[21] and on severely drying fruits[8]. The transition from wrinkles to folds has also been validated in swelling hydrogel bilayers[24,55]. In addition, in a system consisted of a swelling elastomer film on an underlying elastomer substrate ($\mu_f/\mu_s \approx 10^4$), the transition from wrinkle to ridge has been observed[57].

If the adhesion energy between the film and substrate is relatively low (Fig. 6B), multiple delamination patterns have been observed in growing biological systems. For example, growing biofilms may delaminate to form buckle regions to facilitate nutrient transportation[9–11]; the epithelial cells may delaminate due to overcrowd or self-metabolism[25,26]; the swelling hydrogels loosely bonded on substrates may delaminate to form delaminated-buckles[54]. Since the mismatch strains in these phenomena are generally less than 0.4, we stack the three-dimensional phase diagram in the region of $\varepsilon_M = 0.1-0.4$ into a two-dimensional phase diagram (Fig. 6B), where the boundary between delaminated-buckle and other phases is represented by a grey band. From Fig. 6B, it can be seen the reported delaminated-buckle patterns indeed fall in the delaminated-buckle region predicted by the phase diagram.

It should be noted that the phase diagram presented in this paper (Fig. 2) is valid for a wide range of dimensional parameters of growing biological systems. From Fig. 6, Table 1 and Supplementary methods, we can see that the film thickness varies from nanometer to centimeter, the modulus from Pascal to Gigapascal, the adhesion from 10^{-2} J/m^2 to 10^3 J/m^2 and the mismatch strain ε_M from 0 to $\sim$0.6. The cases with excessively large film thickness (>m), large modulus ratio ($\mu_f/\mu_s > 10^5$) and large mismatch strain (>0.6) have not been considered in the phase diagram.

In summary, we present a three-dimensional phase diagram that can quantitatively predict various modes of growth-induced surface instabilities in biological film-substrate structures. By combining theory, computation and experiment, we show that the initially flat biological layers can systematically transform into instability patterns of wrinkle, crease, fold, period-double, ridge, delaminated-buckle and their coexistences, depending on three non-dimensional parameters: mismatch compressive strain, film-substrate modulus ratio, and normalized adhesion energy. The three-dimensional phase diagram offers a unified model for understanding morphogenesis in biological film-substrate structures on a mechanical base. The method for constructing the phase diagram opens new venues to study the formation of more complicated patterns, for example, in multi-layer structures, structures with intrinsic surface curvatures[6,58], and inhomogeneous and/or anisotropic structures[6,8,16,18,59,60]. To the end, the phase diagram can potentially guide the rational design of a variety of biomimetic topographical-structures for engineering applications as diverse as disease therapy[22,24], active cell culture[34], biofouling management[35], tunable superhydrophobicity[36] and flexible electronics[37,38,61].

Methods

Materials. We use an elastomer film (Ecoflex 0010, Smooth-on, USA) with the thickness $\sim$5 mm and the modulus $\sim$10.4 *kPa* as the substrate. The shear modulus of Ecoflex is measured by fitting stress *vs.* strain data from uniaxial tensile tests to the incompressible neo-Hookean law (Micro-Strain Analyzer, TA Instruments, USA). We choose films with a large range of moduli, from $\sim$3 *kPa* to $\sim$0.8 *Gpa*. Below 2 *Mpa*, a silicone elastomer Sylgard 184 (Dow Corning, USA) is spin-casted into thin films with thickness $\sim$200 μm. The shear modulus of Sylgard is varied from 3.1 *kPa* to 1.4 *MPa* by changing its cross-linker concentration. Above 2 *Mpa*, natural rubber ($\sim$16 *Mpa*, 50 μm, McMaster-Carr, USA), low density polyethylene (LPE, $\sim$96 *Mpa*, 25 μm, McMaster-Carr, USA) and Kapton (0.83 *Gpa*, 25 μm, McMaster-Carr, USA) are used to act as the films.

Experimental procedure. To simply induce a mismatch strain between the film and substrate, we first uniaxially pre-stretched the substrate to a prescribed ratio of L_f/L_s (Fig. 1Cii). The Sylgard film is then carefully attached on the pre-stretched substrate by uniformly pressing it on the substrate with two rigid plates, and the bilayer then is baked at an oven with a controlled temperature for 10 min. Thereafter, the pre-stretched substrate is gradually relaxed to the original length with a strain rate around 1×10^{-3} s^{-1}. The surface morphology is captured by a camera (Cannon, USA) with a tilted angel 20°. To enhance the film-substrate adhesion, a very thin layer of uncured Ecoflex can also be smeared on the substrate prior to attaching the films[48,51].

Measurement of the adhesion energy. The adhesion energy between the film and substrate is measured with the peeling test (Supplementary Fig. S12)[62]. A strip of Sylgard film with width b is carefully attached on a prestretched substrate, and the bilayer then is baked at an oven with a controlled temperature for 10 min. A force F is then applied to the Sylgard film to peel off the substrate along an angle θ at a low peeling rate 1×10^{-4} $m\cdot s^{-1}$. The adhesion energy is calculated by $\Gamma = (1-\cos\theta+\varepsilon_d/2)F/b$, where ε_d is the strain in the detached section of the Sylgard film.

Finite element calculations. The finite element calculations (Supplementary Figs S3–S11) are implemented by software ABAQUS 10.1. The film and the substrate are taken to be incompressible neo-Hookean materials with shear moduli μ_f and μ_s respectively. The thickness of the substrate is much larger than that of the film (>20 times). Three methods are used to induce mismatch compressive strains in the films: In the first method, a film-substrate laminate is prestretched by a ratio of L_f/L_s, and then the strain in the film is released, followed by subsequently relaxing the laminate to the original length L_s (Supplementary Figs S3, S4, S5A, S6, S7A and S8–S11). The second method involves swelling of the film in the horizontal direction (Supplementary Figs S5B and S7B), while the third method is shrinking the substrate

in the horizontal direction (Supplementary Figs S5C and S7C). Small force perturbations are introduced to facilitate the initiation of instabilities. The calculation models are discretized by CPE6MH elements, and the result accuracy is ascertained through mesh refinement studies.

1. Ball, P. *The self-made tapestry: pattern formation in nature* (Oxford Univ. Press, Oxford, 1999).
2. Thompson, D. W. *On Growth and Form,* abridged edition edn (Cambridge Univiversity Press, 1917).
3. Cerda, E. & Mahadevan, L. Geometry and physics of wrinkling. *Physical Review Letters* **90**, 074302 (2003).
4. Yin, J., Gerling, G. J. & Chen, X. Mechanical modeling of a wrinkled fingertip immersed in water. *Acta Biomater.* **6**, 1487–1496 (2010).
5. Kücken, M. & Newell, A. A model for fingerprint formation. *Europhys. Lett.* **68**, 141 (2004).
6. Yin, J. *et al.* Stress-driven buckling patterns in spheroidal core/shell structures. *Proc. Natl. Acad. Sci. U.S.A.* **105**, 19132–19135 (2008).
7. Katifori, E. *et al.* Foldable structures and the natural design of pollen grains. *Proceedings of the National Academy of Sciences* **107**, 7635–7639 (2010).
8. Li, B. *et al.* Surface wrinkling patterns on a core-shell soft sphere. *Physical review letters* **106**, 234301 (2011).
9. Wilking, J. N. *et al.* Liquid transport facilitated by channels in Bacillus subtilis biofilms. *Proceedings of the National Academy of Sciences* **110**, 848–852 (2012).
10. Asally, M. *et al.* Localized cell death focuses mechanical forces during 3D patterning in a biofilm. *Proceedings of the National Academy of Sciences* **109**, 18891–18896 (2012).
11. DePas, W. H. *et al.* Iron induces bimodal population development by Escherichia coli. *Proceedings of the National Academy of Sciences* **110**, 2629–2634 (2013).
12. Hohlfeld, E. & Mahadevan, L. Unfolding the sulcus. *Physical review letters* **106**, 105702 (2011).
13. Tallinen, T., Biggins, J. & Mahadevan, L. Surface Sulci in Squeezed Soft Solids. *Physical review letters* **110**, 024302 (2013).
14. Richman, D. P., Stewart, R. M., Hutchinson, J. W. & Caviness Jr, V. S. Mechanical model of brain convolutional development. *Science* **189**, 18–21 (1975).
15. Kriegstein, A., Noctor, S. & Martínez-Cerdeño, V. Patterns of neural stem and progenitor cell division may underlie evolutionary cortical expansion. *Nature Reviews Neuroscience* **7**, 883–890 (2006).
16. Shyer, A. E. *et al.* Villification: How the Gut Gets Its Villi. *Science* **342**, 212–218 (2013).
17. Walton, K. D. *et al.* Hedgehog-responsive mesenchymal clusters direct patterning and emergence of intestinal villi. *Proceedings of the National Academy of Sciences* **109**, 15817–15822 (2012).
18. Amar, M. B. & Jia, F. Anisotropic growth shapes intestinal tissues during embryogenesis. *Proceedings of the National Academy of Sciences* **110**, 10525–10530 (2013).
19. Hannezo, E., Prost, J. & Joanny, J. F. Instabilities of Monolayered Epithelia: Shape and Structure of Villi and Crypts. *Physical Review Letters* **107**, 078104 (2011).
20. Li, B., Cao, Y.-P. & Feng, X.-Q. Growth and surface folding of esophageal mucosa: a biomechanical model. *Journal of biomechanics* **44**, 182–188 (2011).
21. Li, B., Cao, Y.-P., Feng, X.-Q. & Gao, H. Surface wrinkling of mucosa induced by volumetric growth: theory, simulation and experiment. *Journal of the Mechanics and Physics of Solids* **59**, 758–774 (2011).
22. Wiggs, B. R., Hrousis, C. A., Drazen, J. M. & Kamm, R. D. On the mechanism of mucosal folding in normal and asthmatic airways. *Journal of Applied Physiology* **83**, 1814–1821 (1997).
23. Ciarletta, P. Buckling Instability in Growing Tumor Spheroids. *Physical review letters* **110**, 158102 (2013).
24. Dervaux, J., Couder, Y., Guedeau-Boudeville, M.-A. & Amar, M. B. Shape transition in artificial tumors: from smooth buckles to singular creases. *Physical review letters* **107**, 018103 (2011).
25. Eisenhoffer, G. T. *et al.* Crowding induces live cell extrusion to maintain homeostatic cell numbers in epithelia. *Nature* **484**, 546–549 (2012).
26. Marinari, E. *et al.* Live-cell delamination counterbalances epithelial growth to limit tissue overcrowding. *Nature* **484**, 542–545 (2012).
27. Wang, L., Castro, C. E. & Boyce, M. C. Growth strain-induced wrinkled membrane morphology of white blood cells. *Soft Matter* **7**, 11319–11324 (2011).
28. Dervaux, J. & Amar, M. B. Mechanical Instabilities of Gels. *Annu. Rev. Condens. Matter Phys.* **3**, 311–332 (2012).
29. Li, B., Cao, Y.-P., Feng, X.-Q. & Gao, H. Mechanics of morphological instabilities and surface wrinkling in soft materials: a review. *Soft Matter* **8**, 5728–5745 (2012).
30. Burgess, D. R. Morphogenesis of intestinal villi II. Mechanism of formation of previllous ridges. *J. Embryol. Eep. Morph.* **34**, 723–740 (1975).
31. Ben Amar, M. & Goriely, A. Growth and instability in elastic tissues. *Journal of the Mechanics and Physics of Solids* **53**, 2284–2319 (2005).
32. Bradbury, J. Molecular insights into human brain evolution. *PLoS Biol.* **3**, e50 (2005).
33. Akey, J. M. *et al.* Tracking footprints of artificial selection in the dog genome. *Proc. Natl. Acad. Sci. U.S.A.* **107**, 1160–1165 (2010).
34. Kim, J., Yoon, J. & Hayward, R. C. Dynamic display of biomolecular patterns through an elastic creasing instability of stimuli-responsive hydrogels. *Nat. Mater.* **9**, 159–164 (2010).
35. Shivapooja, P. *et al.* Bioinspired Surfaces with Dynamic Topography for Active Control of Biofouling. *Advanced Materials* **25**, 1430–1434 (2013).
36. Zang, J. *et al.* Multifunctionality and control of the crumpling and unfolding of large-area graphene. *Nat. Mater.* **12**, 321–325 (2013).
37. Jiang, H. *et al.* Finite deformation mechanics in buckled thin films on compliant supports. *Proceedings of the National Academy of Sciences* **104**, 15607–15612 (2007).
38. Khang, D. Y., Jiang, H., Huang, Y. & Rogers, J. A. A stretchable form of single-crystal silicon for high-performance electronics on rubber substrates. *Science* **311**, 208–212 (2006).
39. Wang, Q. & Zhao, X. Phase Diagrams of Instabilities in Compressed Film-Substrate Systems. *J. Appl. Mech.* **81**, 051004 (2014).
40. Thompson, J. M. T. & Hunt, G. W. *Elastic instability phenomena* (Wiley Chichester etc., 1984).
41. Ericksen, J. L. *Introduction to the Thermodynamics of Solids* (Springer, 1998).
42. Abeyaratne, R. *Evolution of phase transitions: a continuum theory* (Cambridge University Press, 2006).
43. Hong, W., Zhao, X. & Suo, Z. Formation of creases on the surfaces of elastomers and gels. *Applied Physics Letters* **95**, 111901-111901-111903 (2009).
44. Wang, Q., Zhang, L. & Zhao, X. Creasing to Cratering Instability in Polymers under Ultrahigh Electric Fields. *Physical review letters* **106**, 118301 (2011).
45. Brau, F. *et al.* Multiple-length-scale elastic instability mimics parametric resonance of nonlinear oscillators. *Nature Physics* **7**, 56–60 (2010).
46. Sun, J. Y. *et al.* Folding wrinkles of a thin stiff layer on a soft substrate. *Proc. R. Soc. A* **468**, 932–953 (2012).
47. Vella, D. *et al.* The macroscopic delamination of thin films from elastic substrates. *Proceedings of the National Academy of Sciences* **106**, 10901–10906 (2009).
48. Cai, S., Chen, D., Suo, Z. & Hayward, R. C. Creasing instability of elastomer films. *Soft Matter* **8**, 1301–1304 (2012).
49. Cao, Y. & Hutchinson, J. W. Wrinkling phenomena in neo-Hookean film/substrate bilayers. *Journal of applied mechanics* **79**, 1019 (2012).
50. Chen, X. & Hutchinson, J. W. Herringbone buckling patterns of compressed thin films on compliant substrates. *Journal of applied mechanics* **71**, 597–603 (2004).
51. Chen, D., Cai, S., Suo, Z. & Hayward, R. C. Surface Energy as a Barrier to Creasing of Elastomer Films: An Elastic Analogy to Classical Nucleation. *Physical review letters* **109**, 38001 (2012).
52. Yoon, J., Kim, J. & Hayward, R. C. Nucleation, growth, and hysteresis of surface creases on swelled polymer gels. *Soft Matter* **6**, 5807–5816 (2010).
53. Trujillo, V., Kim, J. & Hayward, R. C. Creasing instability of surface-attached hydrogels. *Soft Matter* **4**, 564–569 (2008).
54. Velankar, S. S., Lai, V. & Vaia, R. A. Swelling-Induced Delamination Causes Folding of Surface-Tethered Polymer Gels. *ACS Appl. Mater. Interfaces* **4**, 24–29 (2012).
55. Sultan, E. & Boudaoud, A. The Buckling of a Swollen Thin Gel Layer Bound to a Compliant Substrate. *J. Appl. Mech.* **75**, 051002–051002 (2008).
56. Tanaka, T. *et al.* Mechanical instability of gels at the phase transition. *Nature* **325**, 796–798 (1987).
57. Breid, D. & Crosby, A. J. Effect of stress state on wrinkle morphology. *Soft Matter* **7**, 4490–4496 (2011).
58. Tallinen, T., Chung, J. Y., Biggins, J. S. & Mahadevan, L. Gyrification from constrained cortical expansion. *Proceedings of the National Academy of Sciences* **111**, 12667–12672 (2014).
59. Grason, G. M. & Davidovitch, B. Universal collapse of stress and wrinkle-to-scar transition in spherically confined crystalline sheets. *Proceedings of the National Academy of Sciences* **110**, 12893–12898 (2013).
60. Wu, Z., Bouklas, N. & Huang, R. Swell-induced surface instability of hydrogel layers with material properties varying in thickness direction. *International Journal of Solids and Structures* **50**, 578–587 (2013).
61. Song, Z. *et al.* Origami lithium-ion batteries. *Nat. Comm.* **5**, 3140 (2014).
62. Kendall, K. The adhesion and surface energy of elastic solids. *J. Phys. D: Appl. Phys.* **4**, 1186 (1971).

Acknowledgments

The work was supported by ONR (No. N00014-14-1-0528) and NSF (No. CMMI-1253495, CMMI-1200515).

Author contributions

Q.W. and X.Z. designed the research. Q.W. performed the experiments. Q.W. and X.Z. developed and analyzed the theoretical models and numerical calculations, interpreted the results, and wrote the manuscript.

Additional information

Supplementary information accompanies this paper at http://www.nature.com/scientificreports

Competing financial interests: The authors declare no competing financial interests.

How to cite this article: Wang, Q. & Zhao, X. A three-dimensional phase diagram of growth-induced surface instabilities. *Sci. Rep.* **5**, 8887; DOI:10.1038/srep08887 (2015).

Supplementary Information for

A Three-Dimensional Phase Diagram of Growth-Induced Surface Instabilities

Qiming Wang[1,2], Xuanhe Zhao[1,2,3*]

[1]Soft Active Materials Laboratory, Department of Mechanical Engineering, Massachusetts Institute of Technology, Cambridge, Massachusetts 02139, USA. [2]Department of Mechanical Engineering and Materials Science, Duke University, Durham, North Carolina 27708, USA. [3]Department of Civil and Environmental Engineering, Massachusetts Institute of Technology, Cambridge, MA 02139, USA.

*Email: zhaox@mit.edu

Supplementary figures

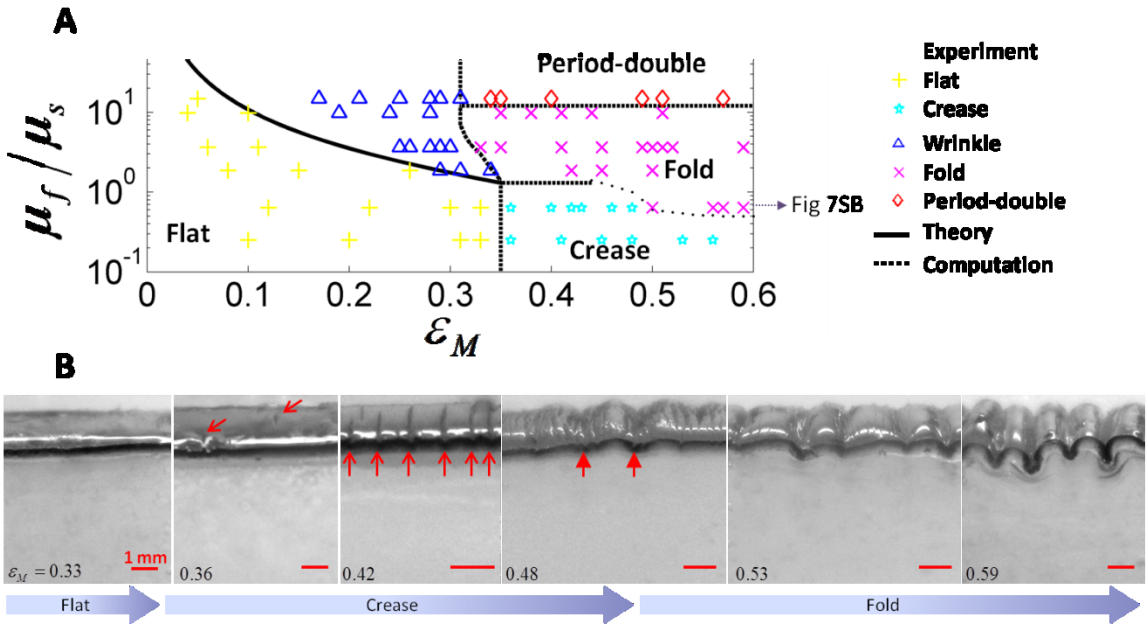

Supplementary Figure S1 | The transition process from creases to folds. (A) Comparison between the calculated phase diagram and experimental results for the transition from creases to folds. (B) Sequences of experimental images to show the transition process from creases to folds with increasing mismatch strain.

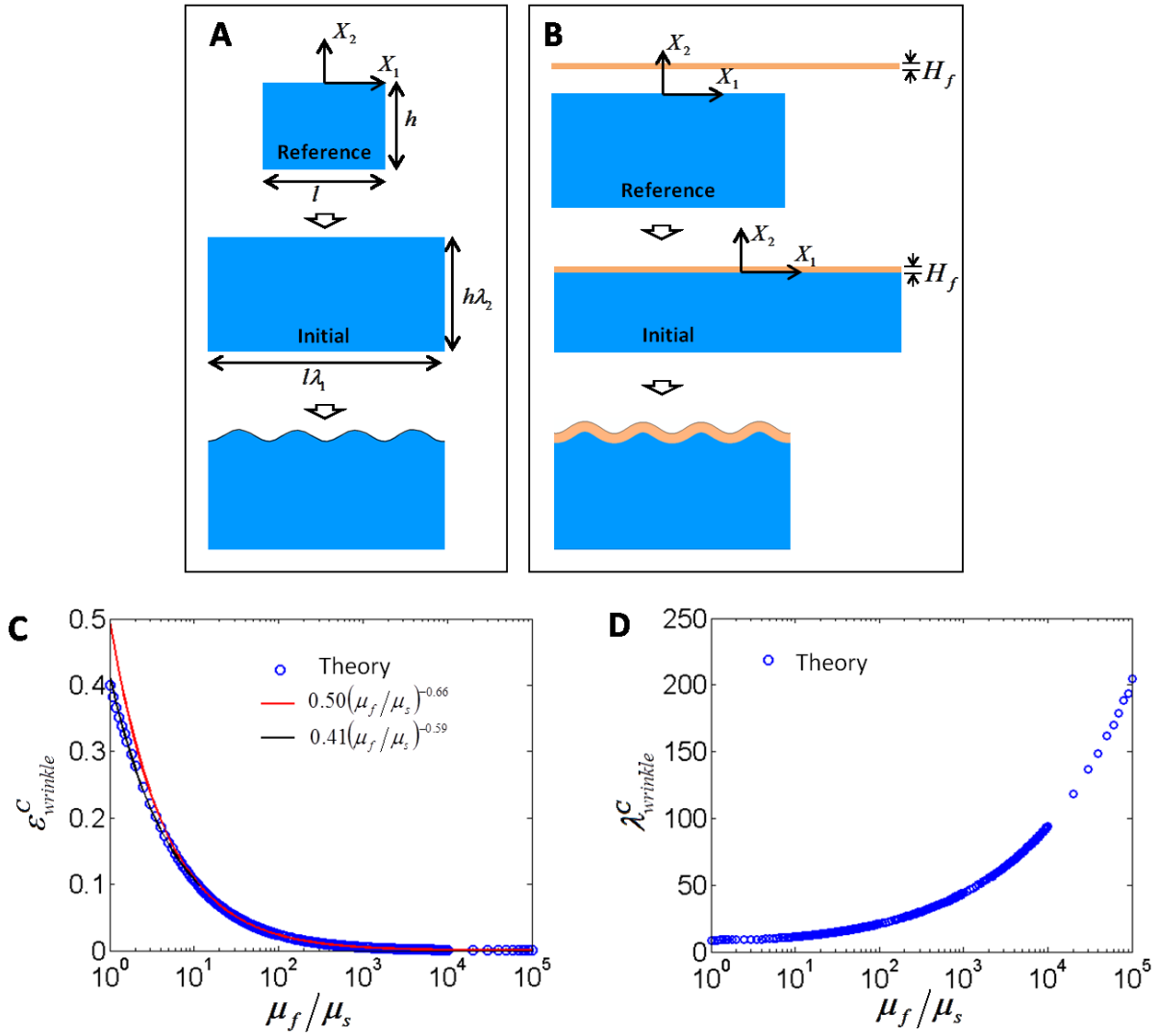

Supplementary Figure S2 | Calculation of the phase boundary between the flat and wrinkled states. Schematics of (A) a neo-Hookean block and (B) a neo-Hookean film-substrate structure. (C) Calculated critical mismatch strain and (D) critical wavelength between flat and wrinkled states as a function of modulus ratio μ_f/μ_s .

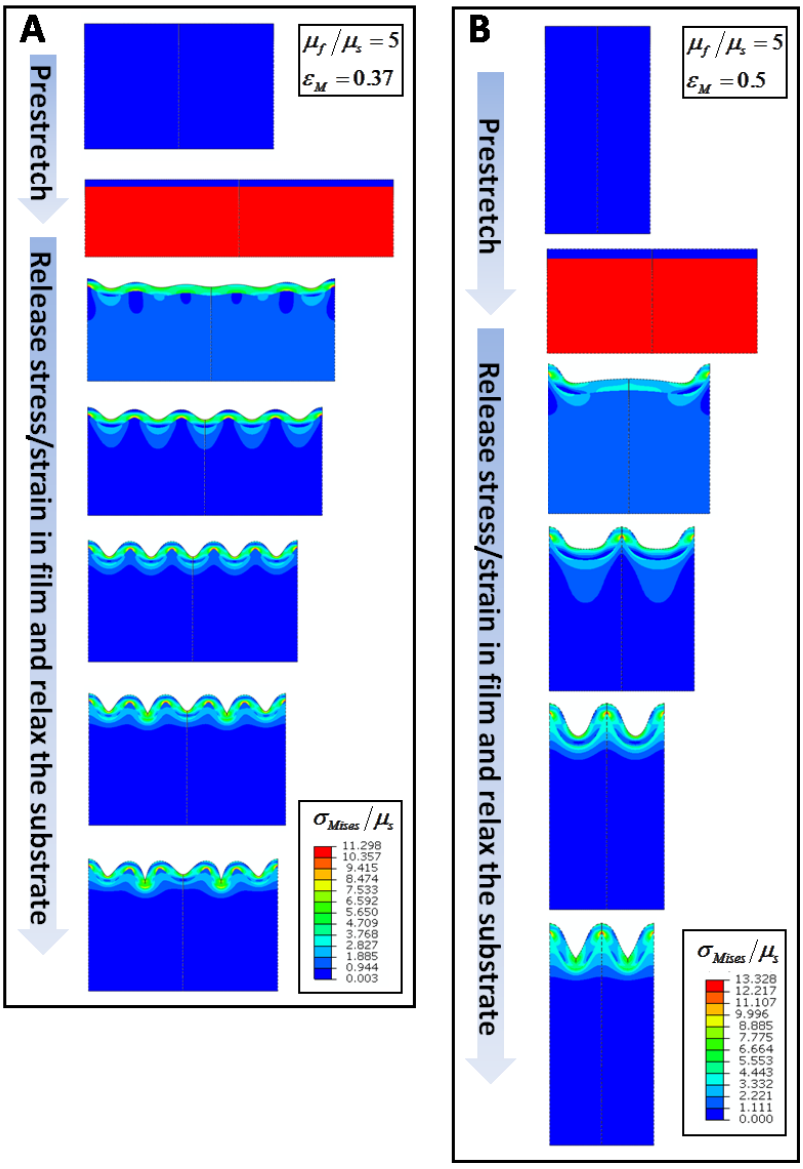

Supplementary Figure S3 | Examples of finite-element models that give the formation of folds in film-substrate structures: (A) $\varepsilon_M = 0.37$, $\mu_f/\mu_s = 5$ **and (B)** $\varepsilon_M = 0.5$, $\mu_f/\mu_s = 5$.

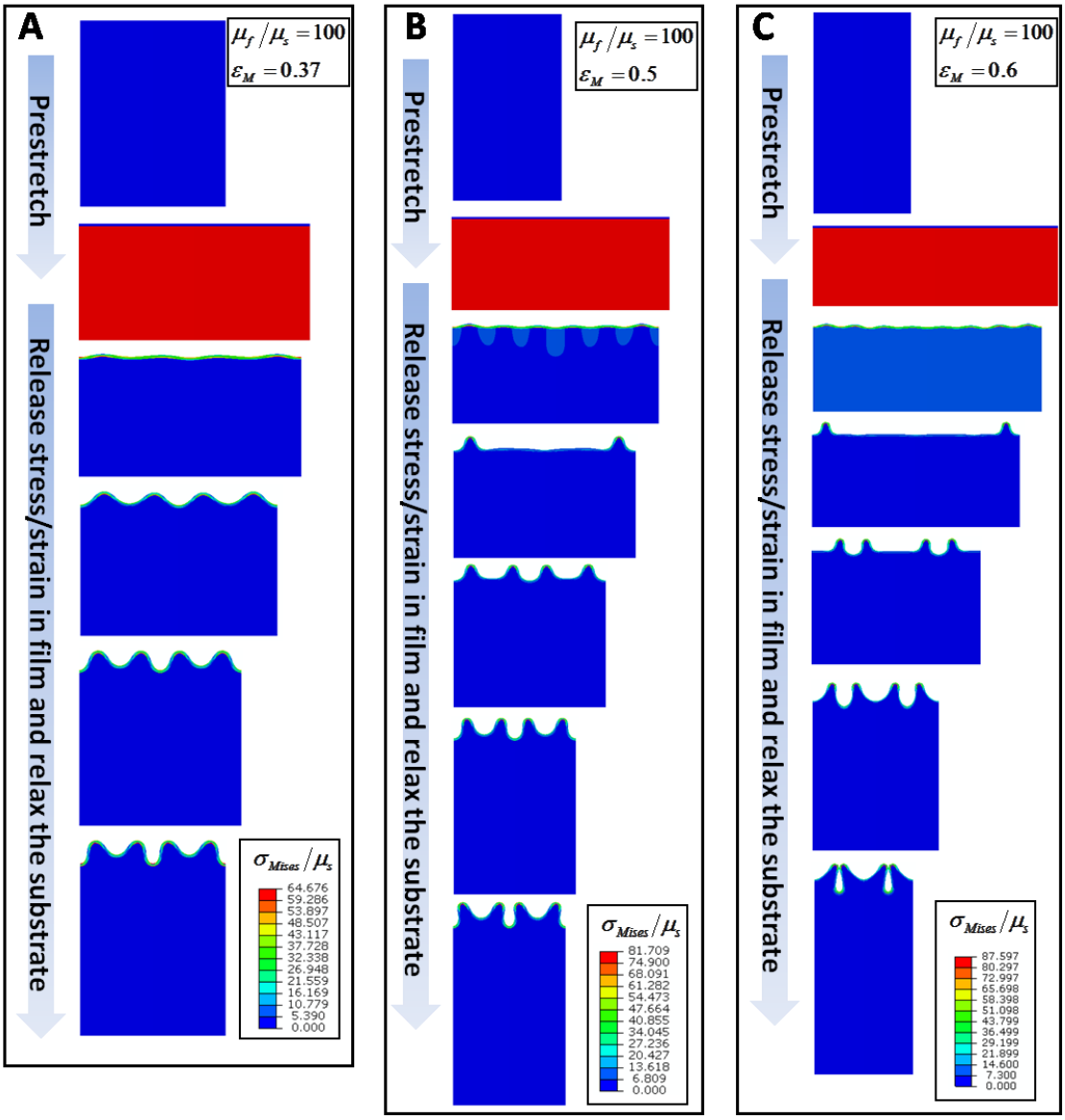

Supplementary Figure S4 | Examples of finite-element models that give the formation of period-doubles in film-substrate structures: (A) $\varepsilon_M = 0.37$, $\mu_f/\mu_s = 100$; **(B)** $\varepsilon_M = 0.5$, $\mu_f/\mu_s = 100$; **and (C)** $\varepsilon_M = 0.6$, $\mu_f/\mu_s = 100$.

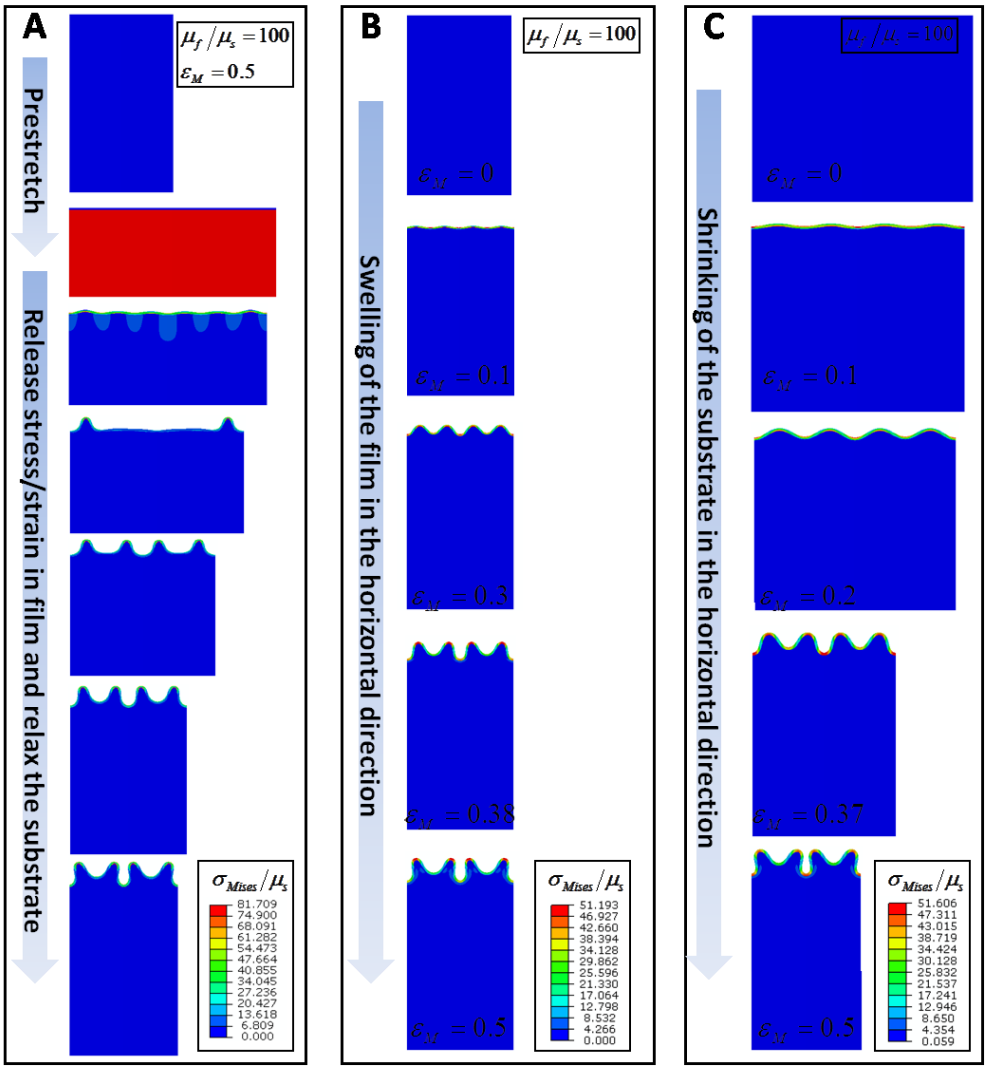

Supplementary Figure S5 | Examples of finite-element models that give the formation of period-doubles in film-substrate structures by following different paths to induce the mismatch strains: (A) substrate pre-stretching and relaxing, (B) film swelling in the horizontal direction, and (C) substrate shrinking in the horizontal direction.

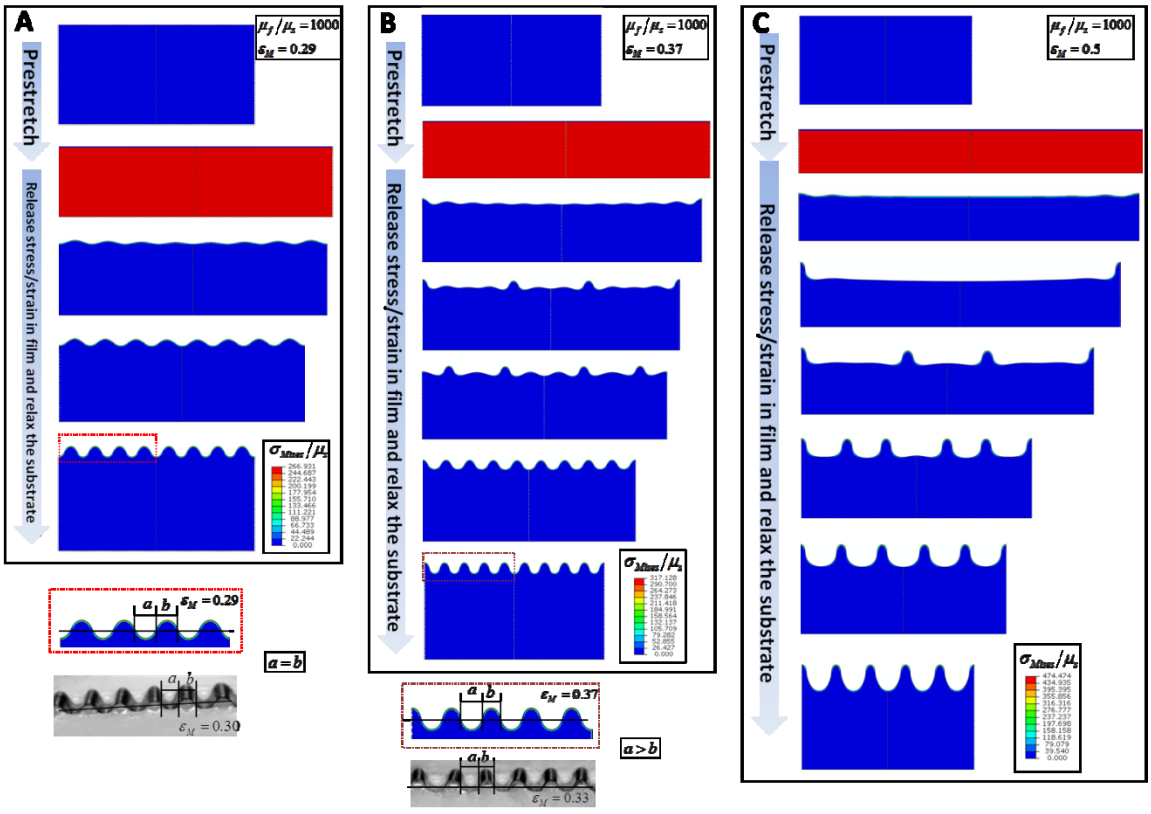

Supplementary Figure S6 | Examples of finite-element models that give the formation of wrinkles in film-substrate structure with (A) $\varepsilon_M = 0.29$, $\mu_f/\mu_s = 1000$; and ridges with (B) $\varepsilon_M = 0.37$, $\mu_f/\mu_s = 1000$and (C) $\varepsilon_M = 0.5$, $\mu_f/\mu_s = 1000$. The half-height-lengths of adjacent wrinkles are equal (a=b) as shown in (A); while the half-height-lengths of adjacent ridges are unequal (b<a) as shown in (B).

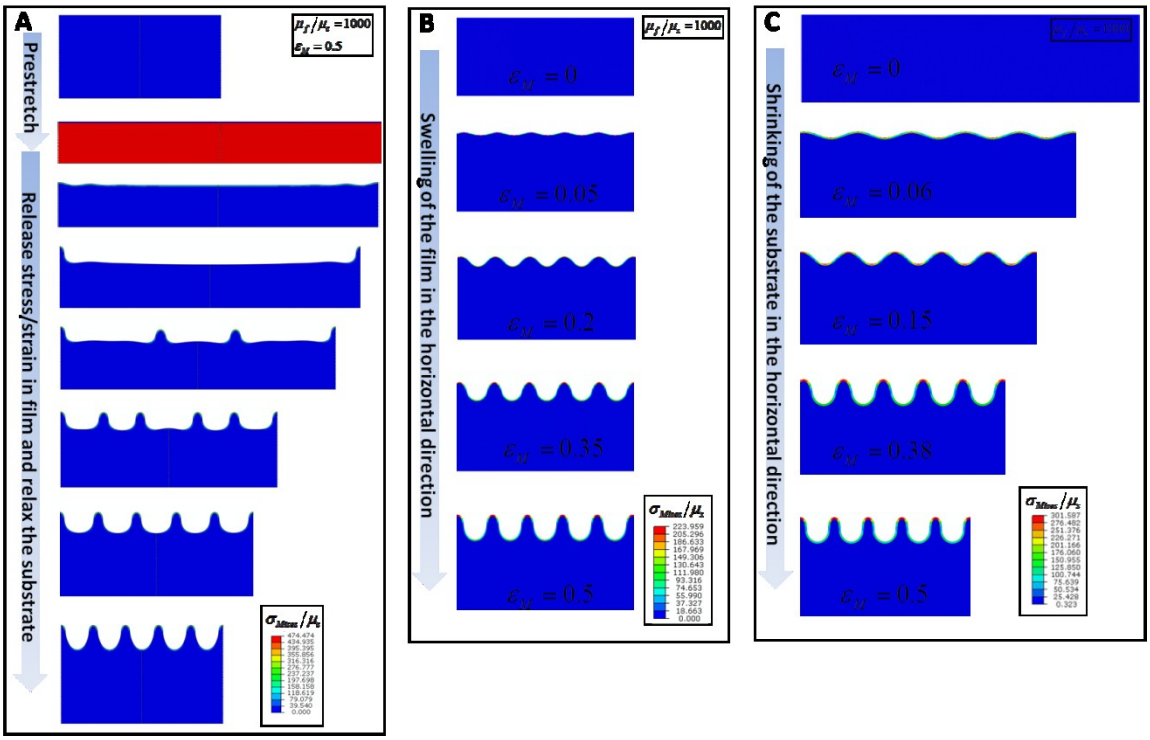

Supplementary Figure S7 | Examples of finite-element models that give the formation of ridges in film-substrate structures by following different paths to induce the mismatch strains: (A) substrate pre-stretching and relaxing, (B) film swelling in the horizontal direction, and (C) substrate shrinking in the horizontal direction.

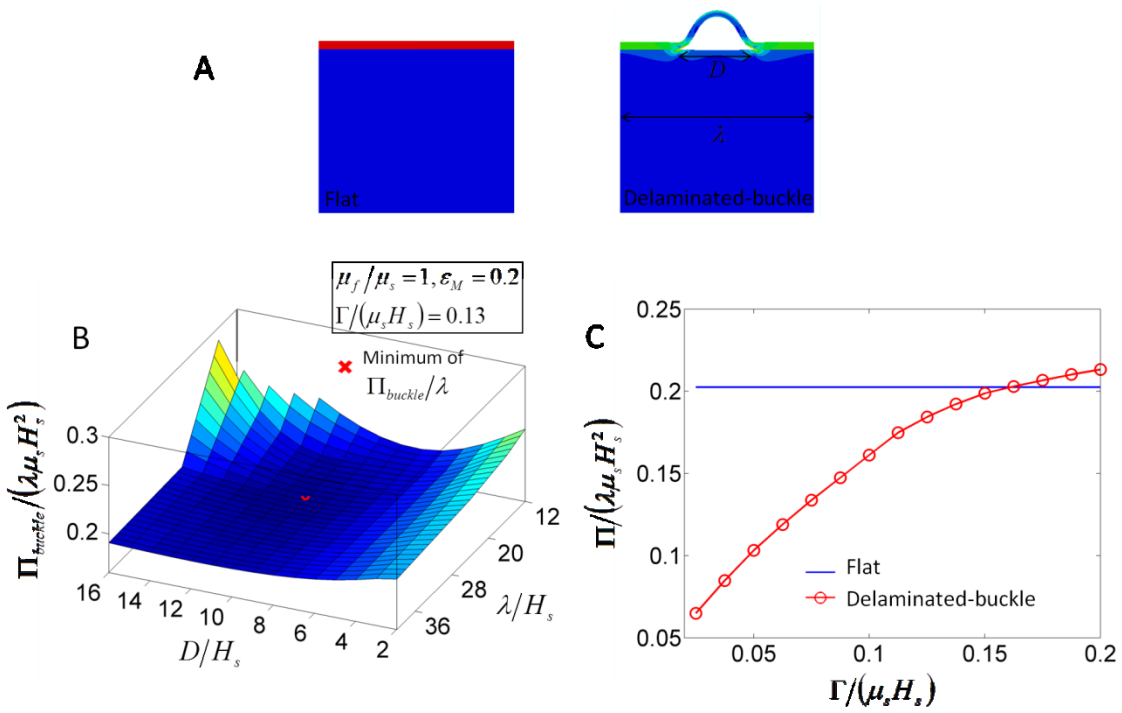

Supplementary Figure S8 | Calculation of the phase boundary between the flat and delaminated-buckled states. (A) Finite-element model of a film-substrate structure at flat and delaminated-buckled states with $\mu_f/\mu_s=1$ and $\varepsilon_M=0.2$. (B) The potential energy per wavelength of the delaminated-buckled state as a function of delamination length D and wavelength λ. The minimum of potential energy per wavelength of the structure is determined by $\partial(\Pi_{buckle}/\lambda)/\partial\lambda=0$ and $\partial(\Pi_{buckle}/\lambda)/\partial D=0$. (C) The potential energy per wavelength of the structure at flat and delaminated-buckled states as functions of the film-substrate adhesion energy. The intersection point ($\Gamma/(\mu_s H_f)=0.158$) between two lines denotes the phase boundary between the flat state and delaminated-buckled state. Therefore, when $\Gamma/(\mu_s H_f)<0.158$, the delaminated-buckled state is the current state of the structure with $\mu_f/\mu_s=1$ and $\varepsilon_M=0.2$; when $\Gamma/(\mu_s H_f)>0.158$, the flat state is the current state.

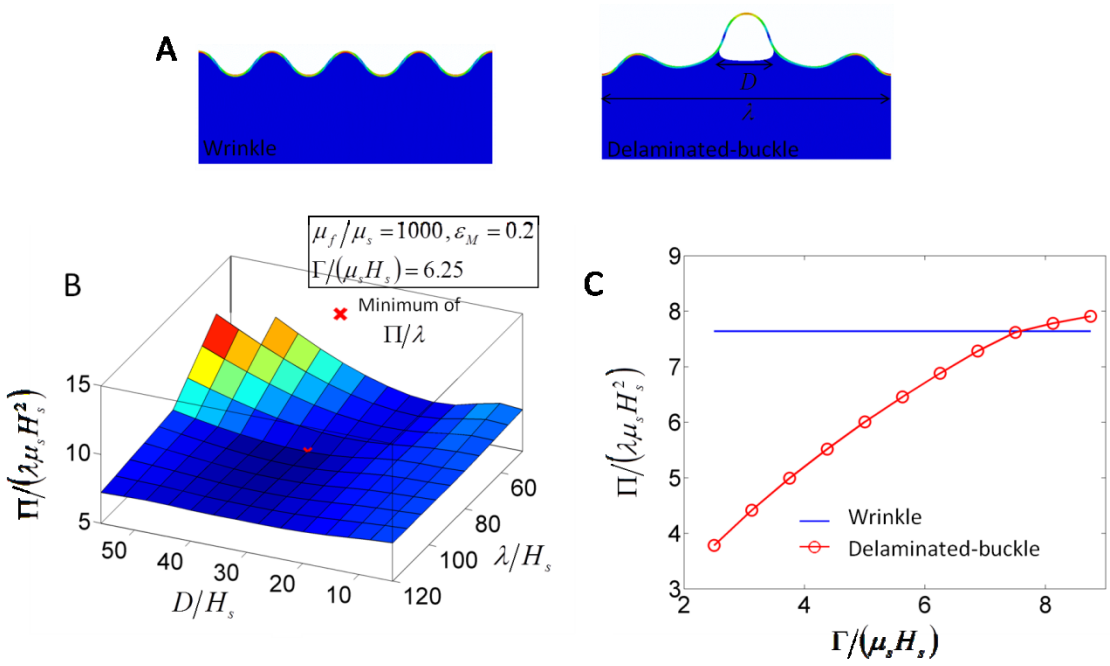

Supplementary Figure S9 | Calculation of the phase boundary between the wrinkled and delaminated-buckled states. (A) Finite-element model of a film-substrate structure at wrinkled and delaminated-buckled states with $\mu_f/\mu_s=1000$ and $\varepsilon_M=0.2$. (B) The potential energy per wavelength of the delaminated-buckled state as a function of delamination length D and wavelength λ. The minimum of potential energy per wavelength of the structure is determined by $\partial(\Pi_{buckle}/\lambda)/\partial\lambda=0$ and $\partial(\Pi_{buckle}/\lambda)/\partial D=0$. (C) The potential energy per wavelength of the structure at wrinkled and delaminated-buckled states as functions of the film-substrate adhesion energy. The intersection point ($\Gamma/(\mu_s H_f)=7.5$) between two lines denotes the phase boundary between the flat state and delaminated-buckled state. Therefore, when $\Gamma/(\mu_s H_f)<7.5$, the delaminated-buckled state is the current state of the structure with $\mu_f/\mu_s=1000$ and $\varepsilon_M=0.2$; when $\Gamma/(\mu_s H_f)>7.5$, the wrinkled state is the current state.

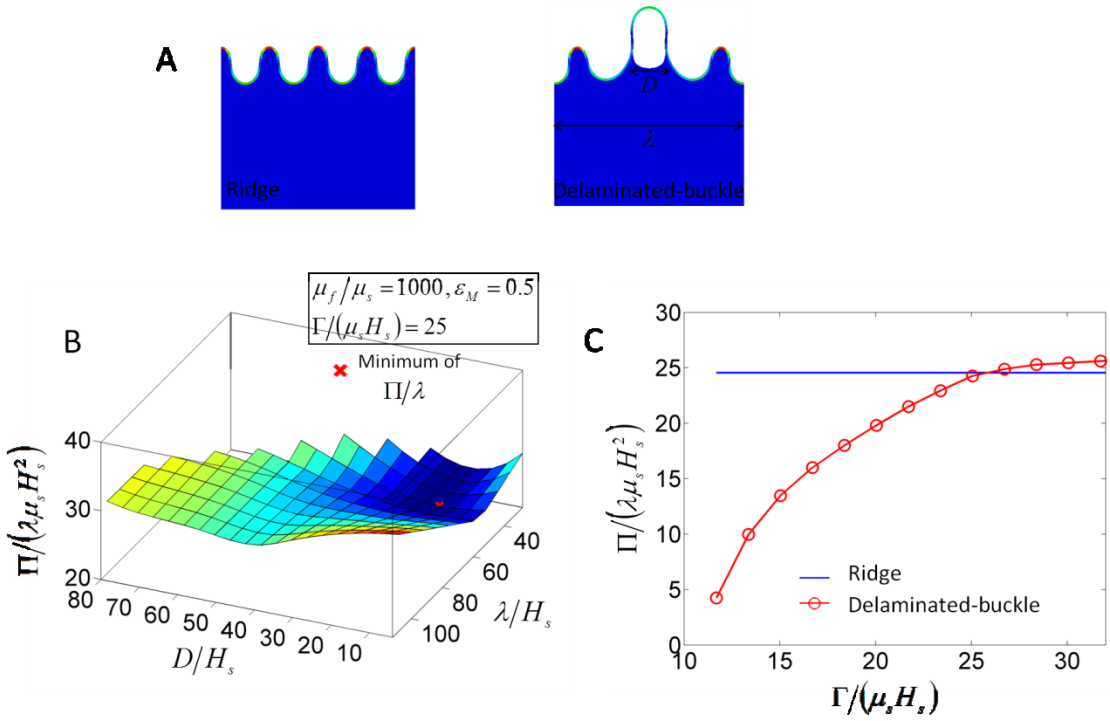

Supplementary Figure S10 | Calculation of the phase boundary between the ridged and delaminated-buckled states. (A) Finite-element model of a film-substrate structure at ridged state and delaminated-buckled state with $\mu_f/\mu_s=1000$ and $\varepsilon_M=0.5$. (B) The potential energy per wavelength of the delaminated-buckled state as a function of delamination length D and wavelength λ. The minimum of potential energy per wavelength of the structure is determined by $\partial(\Pi_{buckle}/\lambda)/\partial\lambda=0$ and $\partial(\Pi_{buckle}/\lambda)/\partial D=0$. (C) The potential energy per wavelength of the structure at ridged and delaminated-buckled states as functions of the film-substrate adhesion energy. The intersection point ($\Gamma/(\mu_s H_f)=25$) between two lines denotes the phase boundary between the ridged state and delaminated-buckled state. Therefore, when $\Gamma/(\mu_s H_f)<25$, delaminated-buckled state is the current state of the structure with $\mu_f/\mu_s=1000$ and $\varepsilon_M=0.5$; when $\Gamma/(\mu_s H_f)>25$, the ridged state is the current state.

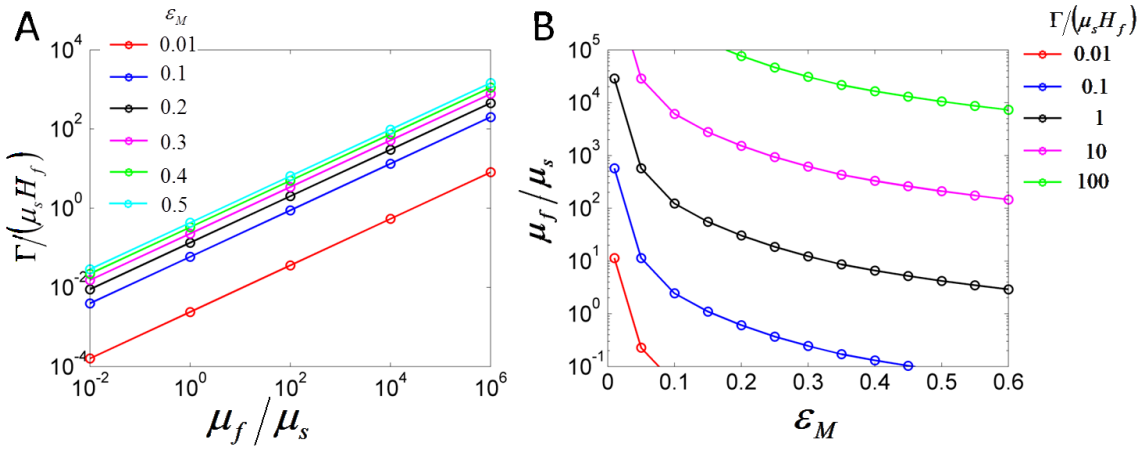

Supplementary Figure S11 | Calculation of the phase boundary between the delaminated-buckled state and un-delaminated state. (A) The calculated critical values of normalized adhesion energy $\Gamma/(\mu_s H_f)$ on the phase boundary between the delaminated-buckled state and un-delaminated state as functions of modulus ratio and mismatch strain. (B) Re-plot of (A) as the calculated critical values of modulus ratio on the phase boundary as functions of mismatch strain and normalized adhesion energy.

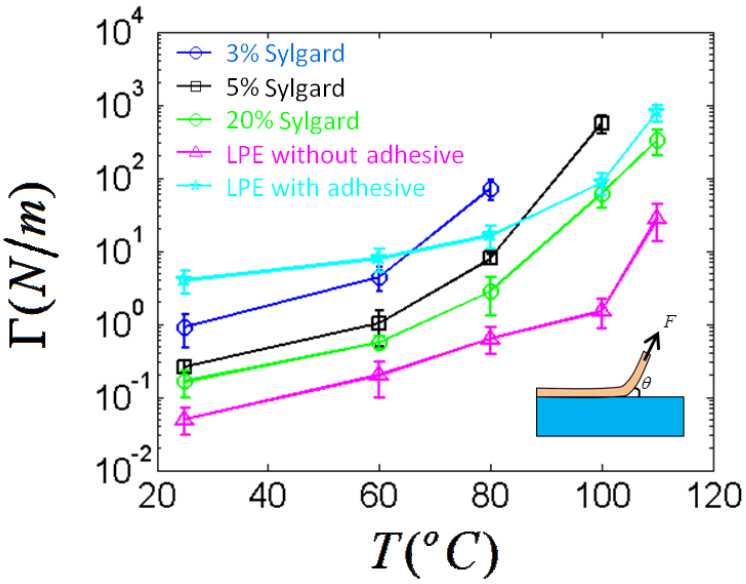

Supplementary Figure S12 | The measured adhesion energy between different films and Ecoflex substrates for different baking temperatures. The adhesive layer is a very thin layer of uncured Ecoflex smeared on the substrate prior to attaching the film.

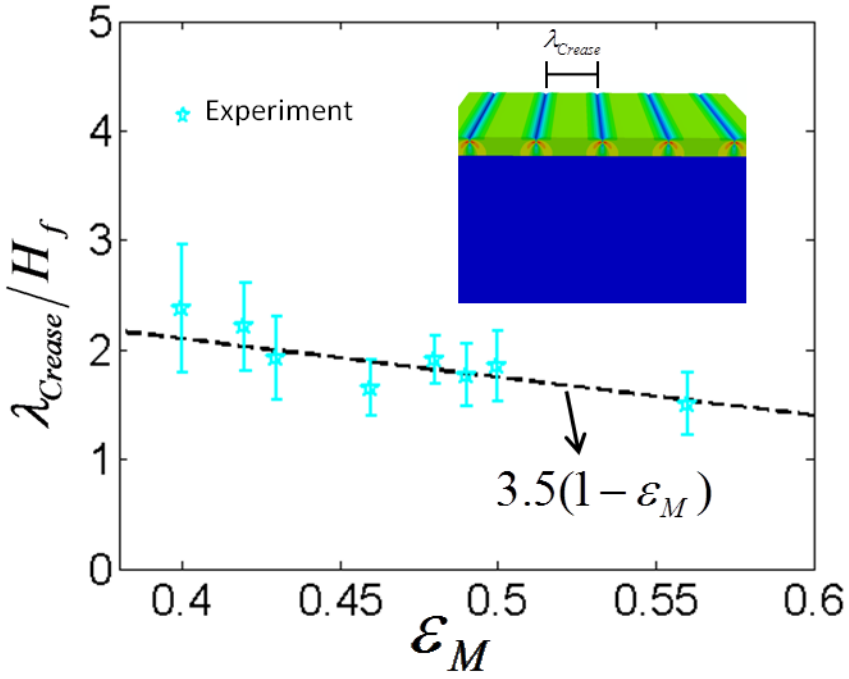

Supplementary Figure S13| Wavelength of creases varied with mismatch strains.

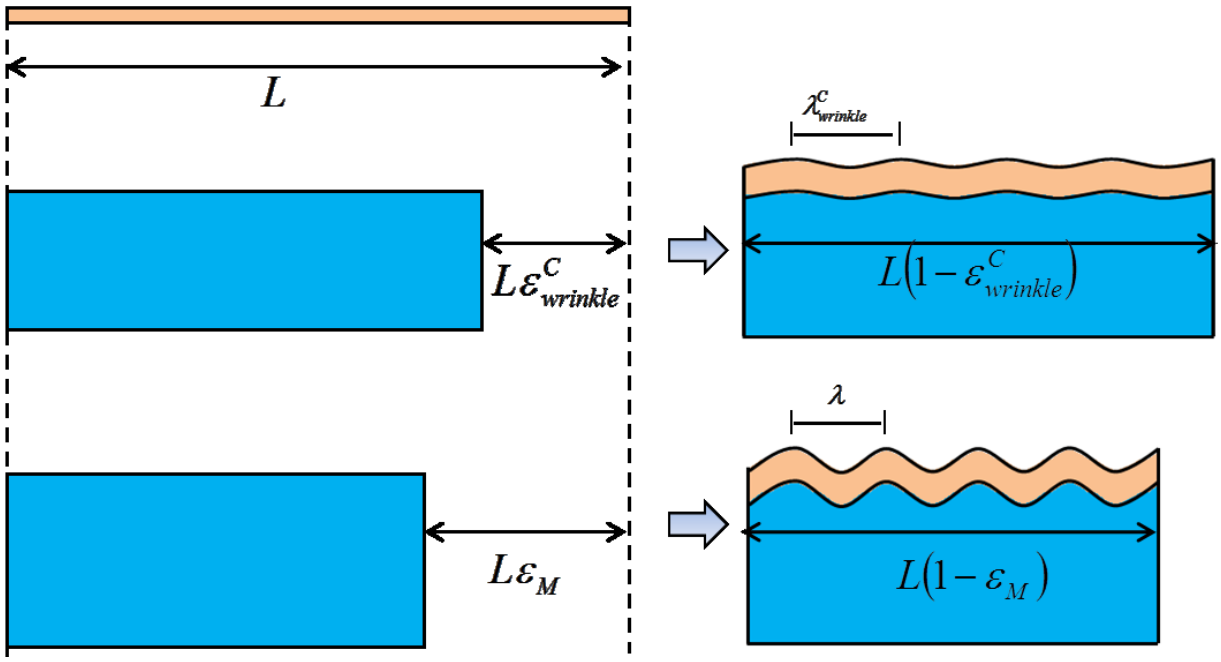

Supplementary Figure S14| Schematics of the modified accordion model. As the mismatch strain increases due to the shrinkage of substrate, the number of undulations in wrinkles maintains constant but the wavelength of the wrinkles decreases accordingly.

Supplementary Methods

Analysis of wrinkling instability

Following Hutchinson and Cao [1-3] and Koiter [4], a stability analysis for the mismatch-strain-induced wrinkling instability is re-derived here to calculate the critical mismatch strain for flat-wrinkling transition in film-substrate systems with varied modulus ratio μ_f / μ_s .

Base solutions of a single neo-Hookean block

We first consider a rectangular incompressible neo-Hookean block, and take its undeformed state as the reference state in the Lagrangian coordinate X_1, X_2 and X_3 as shown in **Supplementary Figure S2A**. The top surface of the block is at $X_2=0$. The block is then homogeneously deformed by stretches λ_1, λ_2 and λ_3 along three axes, where λ_3 will be fixed in future plane-strain deformation. This homogeneously deformed state is denoted as the initial state of the block.

Next, we will perturb this initial state with small and periodic deformation. Assuming the solutions we seek follow periodic forms with a wavelength l in the reference state in X_1 direction, we take the analysis domain in X_1 direction as $0 \le X_1 \le l$. Since the thickness of the block in X_2 direction is h at the reference state, the analysis domain in X_2 direction is $-h \le X_2 \le 0$.

The deformation gradient tensor for the block at the initial state is

$$\mathbf{F}^0 = \begin{bmatrix} \lambda_1 & & \\ & \lambda_2 & \\ & & \lambda_3 \end{bmatrix} \tag{S1}$$

The strain energy density of this initial state is

$$\varphi_0 = \frac{1}{2}\mu\left(tr\mathbf{F}^{0\mathrm{T}}\mathbf{F}^0 - 3\right) = \frac{1}{2}\mu\left(\lambda_1^2 + \lambda_2^2 + \lambda_3^2 - 3\right) \tag{S2}$$

where μ is the shear modulus of the neo-Hookean block. When an incremental displacement U_1 and U_2 is imposed along X_1 and X_2 directions onto the initial state, the resultant deformation gradient of the current state can be expressed as

$$\mathbf{F}=\begin{bmatrix}\lambda_1+U_{1,1} & U_{1,2} & 0\\ U_{2,1} & \lambda_2+U_{2,2} & 0\\ 0 & 0 & \lambda_3\end{bmatrix} \tag{S3}$$

where $U_{1,1}=\partial U_1/\partial X_1$, $U_{2,2}=\partial U_2/\partial X_2$, $U_{1,2}=\partial U_1/\partial X_2$ and $U_{2,1}=\partial U_2/\partial X_1$. The strain energy density of the current state is

$$\varphi=\frac{1}{2}\mu\left(tr\mathbf{F}^{\mathrm{T}}\mathbf{F}-3\right)=\frac{1}{2}\mu\left[\left(\lambda_1+U_{1,1}\right)^2+\left(\lambda_2+U_{2,2}\right)^2+\left(U_{2,1}\right)^2+\left(U_{1,2}\right)^2+\lambda_3^2-3\right] \tag{S4}$$

The difference in strain energy densities between the current and initial states is

$$\varphi-\varphi_0=\mu\left[\lambda_1U_{1,1}+\lambda_2U_{2,2}+\frac{1}{2}\left(U_{1,1}^2+U_{2,2}^2+U_{2,1}^2+U_{1,2}^2\right)\right] \tag{S5}$$

The incompressibility condition, $\det(\mathbf{F})=1$, further imposes

$$\Omega(\lambda,U)=\lambda_2U_{1,1}+\lambda_1U_{2,2}+U_{1,1}U_{2,2}-U_{2,1}U_{1,2}=0 \tag{S6}$$

Therefore, the potential energy difference between current and initial states can be expressed as

$$\Phi=\mu\int_0^l\int_{-h}^0\begin{bmatrix}\lambda_1U_{1,1}+\lambda_2U_{2,2}+\frac{1}{2}\left(U_{1,1}^2+U_{2,2}^2+U_{2,1}^2+U_{1,2}^2\right)\\ -q\left(\lambda_2U_{1,1}+\lambda_1U_{2,2}+U_{1,1}U_{2,2}-U_{2,1}U_{1,2}\right)\end{bmatrix}dX_1dX_2 \tag{S7}$$

where $q(X_1,X_2)$ is a Lagrangian multiplier.

To eliminate terms linear in U_i (i=1, 2) in **Supplementary Eq. S7**, we denote $q = r + Q$ with $r \equiv \lambda_2/\lambda_1$, where $Q(X_1, X_2)$ has the same periodicity as U_i. We further assume U_i follows a periodic form with a wavelength l in X_1 direction, so $U_{1,1}$ integrates to zero by periodicity. Consequently, we obtain

$$\Phi = \mu \int_0^l \int_{-h}^0 I(\lambda_i, U_i, Q, r) dX_1 dX_2 \tag{S8}$$

where

$$I = \frac{1}{2}\left(U_{1,1}^2 + U_{2,2}^2 + U_{2,1}^2 + U_{1,2}^2\right) - Q\left(\lambda_2 U_{1,1} + \lambda_1 U_{2,2}\right) - (r+Q)\left(U_{1,1}U_{2,2} - U_{2,1}U_{1,2}\right) \tag{S9}$$

By using variation method, we vary U_1, U_2 and Q by η, ζ and δQ and obtain

$$\begin{aligned} \delta I = {} & \left(U_{1,1}\eta_{,1} + U_{2,2}\zeta_{,2} + U_{2,1}\zeta_{,1} + U_{1,2}\eta_{,2}\right) - \delta Q\left(\lambda_2 U_{1,1} + \lambda_1 U_{2,2} + U_{1,1}U_{2,2} - U_{2,1}U_{1,2}\right) \\ & - Q\left(\lambda_2 \eta_{,1} + \lambda_1 \zeta_{,2}\right) - (r+Q)\left(U_{1,1}\zeta_{,2} + \eta_{,1}U_{2,2} - \zeta_{,1}U_{1,2} - U_{2,1}\eta_{,2}\right) \end{aligned} \tag{S10}$$

We express the variation of the potential energy difference as

$$\delta\Phi = \mu \int_0^l \int_{-h}^0 \delta I dX_1 dX_2 = 0 \tag{S11}$$

Through integration by parts, we reach

$$\begin{aligned} \int_0^l \int_{-h}^0 \delta I dX_1 dX_2 = {} & -\int_0^l \int_{-h}^0 \eta\left[U_{1,11} + U_{1,22} - \left(Q_{,1}U_{2,2} - Q_{,2}U_{2,1}\right) - \lambda_2 Q_{,1}\right] dX_1 dX_2 - \\ & \int_0^l \int_{-h}^0 \zeta\left[U_{2,11} + U_{2,22} - \left(Q_{,1}U_{1,2} - Q_{,2}U_{1,1}\right) - \lambda_1 Q_{,2}\right] dX_1 dX_2 - \\ & \int_0^l \int_{-h}^0 \delta Q\left[\lambda_2 U_{1,1} + \lambda_1 U_{2,2} + U_{1,1}U_{2,2} - U_{1,2}U_{2,1}\right] dX_1 dX_2 + BT \end{aligned} \tag{S12}$$

where *BT* denotes the boundary terms that can be expressed as

$$BT = \int_{-h}^{0} \left[U_{1,1}\eta - Q\lambda_2\eta - (r+Q)U_{2,2}\eta \right]_0^l dX_2 + \int_0^l \left[U_{1,2}\eta + (r+Q)U_{2,1}\eta \right]_{-h}^{0} dX_1 + \int_{-h}^{0} \left[U_{2,1}\zeta + (r+Q)U_{1,2}\zeta \right]_0^l dX_2 + \int_0^l \left[U_{2,2}\eta - Q\lambda_1\zeta + (r+Q)U_{1,1}\eta \right]_{-h}^{0} dX_1 \quad \text{(S13)}$$

Equilibrium requires $\delta\Phi$ to be 0 for arbitrary η, ζ and δQ, so we obtain a set of differential equations as from **Supplementary Eqs. S11** and **S12**,

$$\begin{cases} U_{1,11} + U_{1,22} - \left(Q_{,1}U_{2,2} - Q_{,2}U_{2,1} \right) - \lambda_2 Q_{,1} = 0 \\ U_{2,11} + U_{2,22} - \left(Q_{,1}U_{1,2} - Q_{,2}U_{1,1} \right) - \lambda_1 Q_{,2} = 0 \\ \lambda_2 U_{1,1} + \lambda_1 U_{2,2} + U_{1,1}U_{2,2} - U_{1,2}U_{2,1} = 0 \end{cases} \quad \text{(S14)}$$

Focusing on a linear perturbation analysis, we further neglect the quadratic terms in **Supplementary Eq. S14** and thus obtain

$$\begin{cases} U_{1,11} + U_{1,22} - \lambda_2 Q_{,1} = 0 \\ U_{2,11} + U_{2,22} - \lambda_1 Q_{,2} = 0 \\ \lambda_2 U_{1,1} + \lambda_1 U_{2,2} = 0 \end{cases} \quad \text{(S15)}$$

Supplementary Eq. S15 can be further written as

$$\begin{cases} U_{1,11} + U_{1,22} - r\lambda_1 Q_{,1} = 0 \\ U_{2,11} + U_{2,22} - \lambda_1 Q_{,2} = 0 \\ rU_{1,1} + U_{2,2} = 0 \end{cases} \quad \text{(S16)}$$

We are looking for the following periodic solutions

$$\begin{cases} U_1 = Fe^{ksX_2} \sin(kX_1) \\ U_2 = Ge^{ksX_2} \cos(kX_1) \\ \lambda_1 Q = kHe^{ksX_2} \cos(kX_1) \end{cases} \quad \text{(S17)}$$

By plugging **Supplementary Eq. S17** in **Supplementary Eq. S16**, we obtain

$$\begin{bmatrix} k^2\left(s^2-1\right) & 0 & k^2 r \\ 0 & k^2\left(s^2-1\right) & -k^2 s \\ rk & sk & 0 \end{bmatrix}\begin{bmatrix} F \\ G \\ H \end{bmatrix}=0. \tag{S18}$$

We solve it as

$$\begin{cases} s=r, F=-G, H=Gr^{-1}\left(r^2-1\right) \\ s=1, F=-Gr^{-1}, H=0 \\ s=-r, F=G, H=-Gr^{-1}\left(r^2-1\right) \\ s=-1, F=Gr^{-1}, H=0 \end{cases}. \tag{S19}$$

Based on the solutions in **Supplementary Eq. S19**, we express the general solution for the incremental displacement as

$$\left(U_1, U_2\right)=\left(\overline{U}_1 \sin kX_1, \overline{U}_2 \cos kX_1\right), \tag{S20}$$

$$\begin{cases} \overline{U}_1=-c_1 e^{rkX_2}-c_2 r^{-1} e^{kX_2}+c_3 e^{-rkX_2}+c_4 r^{-1} e^{-kX_2} \\ \overline{U}_2=c_1 e^{rkX_2}+c_2 e^{kX_2}+c_3 e^{-rkX_2}+c_4 e^{-kX_2} \end{cases} \tag{S21}$$

where c_1, c_2, c_3 and c_4 are undetermined parameters.

We denote N_{ij} as the nominal stress in the *j* direction acting on the face normal to *i* direction. The virtual work associated with $\delta U_{j,i}$ can be expressed as

$$N_{ij}\delta U_{j,i}=N_{11}\delta U_{1,1}+N_{12}\delta U_{2,1}+N_{21}\delta U_{1,2}+N_{22}\delta U_{2,2} \tag{S22}$$

The virtual work can also be expressed as

$$\begin{aligned} \mu\delta I=&\mu\left[U_{1,1}-\lambda_2 Q-\left(r+Q\right)U_{1,1}\right]\delta U_{1,1}+\mu\left[U_{2,1}+\left(r+Q\right)U_{1,2}\right]\delta U_{2,1}+ \\ &\mu\left[U_{1,2}+\left(r+Q\right)U_{2,1}\right]\delta U_{1,2}+\mu\left[U_{2,2}-\lambda_1 Q-\left(r+Q\right)U_{1,1}\right]\delta U_{2,2} \end{aligned} \tag{S23}$$

By considering $N_{ij}\delta U_{j,i} = \mu\delta I$, we can calculate the nominal stress on the surface as

$$(N_{21}, N_{22}) = (\overline{N}_{21}\sin kX_1, \overline{N}_{22}\cos kX_1) \tag{S24}$$

where

$$\begin{cases} \overline{N}_{21} = -\mu k\left[2c_1 re^{rkX_2} + c_2 r^{-1}\left(r^2+1\right)e^{kX_2} + 2c_3 re^{-rkX_2} + c_4 r^{-1}\left(r^2+1\right)e^{-kX_2}\right] \\ \overline{N}_{22} = -\mu k\left[-c_1 r^{-1}\left(r^2+1\right)e^{rkX_2} - 2c_2 e^{kX_2} + c_3 r^{-1}\left(r^2+1\right)e^{-rkX_2} + 2c_4 e^{-kX_2}\right] \end{cases} \tag{S25}$$

Wrinkling of a neo-Hookean film-substrate structure

Next, we consider a structure consisting of a film with modulus μ_f and thickness H_f bonded on a prestretched semi-infinite substrate with modulus μ_s (**Supplementary Fig. S2b**). The substrate is pre-stretched by $(\lambda_{1s}^0, \lambda_{2s}^0, \lambda_{3s}^0) = (\lambda_p, 1/\lambda_p, 1)$ along X_1, X_2 and X_3 directions, bonded to the film, and then relaxed. Both the film and the substrate are assumed to undergo homogenous deformation at initial state, and the stretches in the film are $(\lambda_{1f}, \lambda_{2f}, 1)$, and in the substrate are $(\lambda_{1s}, \lambda_{2s}, 1) = (\lambda_p\lambda_{1f}, \lambda_{2f}/\lambda_p, 1)$ in X_1, X_2 and X_3 directions. We further denote

$$r_f = r = \lambda_{2f}/\lambda_{1f} \text{ in the film, and} \tag{S26a}$$

$$r_s = \lambda_{2s}/\lambda_{1s} = r/\lambda_p^2 \text{ in the substrate.} \tag{S26b}$$

In the film domain $0 \le X_2 \le H_f$, the traction stress on the free surface should be vanishing, thus

$$(\overline{N}_{21}, \overline{N}_{22}) = 0 \text{ at } X_2 = H_f \tag{S27}$$

From **Supplementary Eqs S27** and S**25**, we have

$$\begin{cases} 2c_1 re^{rkH_f} + c_2 r^{-1}\left(r^2+1\right)e^{kH_f} + 2c_3 re^{-rkH_f} + c_4 r^{-1}\left(r^2+1\right)e^{-kH_f} = 0 \\ -c_1 r^{-1}\left(r^2+1\right)e^{rkH_f} - 2c_2 e^{kH_f} + c_3 r^{-1}\left(r^2+1\right)e^{-rkH_f} + 2c_4 e^{-kH_f} = 0 \end{cases} \text{ at } X_2 = H_f \tag{S28}$$

On the film-substrate interface $X_2 = 0^{\pm}$, the displacement and surface traction should be continuous, and therefore

$$\frac{1}{\lambda_{1f}\lambda_{3f}}\left(\overline{N}_{21}, \overline{N}_{22}\right)^{+} = \frac{1}{\lambda_{1s}\lambda_{3s}}\left(\overline{N}_{21}, \overline{N}_{22}\right)^{-} \text{ at } X_2 = 0 \tag{S29}$$

where

$$\left(\overline{N}_{21}, \overline{N}_{22}\right)^{+} = \left(2c_1 r + c_2 r^{-1}\left(r^2+1\right) + 2c_3 r + c_4 r^{-1}\left(r^2+1\right), -c_1 r^{-1}\left(r^2+1\right) - 2c_2 + c_3 r^{-1}\left(r^2+1\right) + 2c_4\right) \tag{S30}$$

$$\left(\overline{N}_{21}, \overline{N}_{22}\right)^{-} = \left(2c_1 r + c_2 r_s^{-1}\left(r_s^{\,2}+1\right) + 2c_3 r_s + c_4 r_s^{-1}\left(r_s^{\,2}+1\right), -c_1 r_s^{-1}\left(r_s^{\,2}+1\right) - 2c_2 + c_3 r_s^{-1}\left(r_s^{\,2}+1\right) + 2c_4\right) \tag{S31}$$

$$\left(\overline{U}_1, \overline{U}_2\right)^{+} = \left(\overline{U}_1, \overline{U}_2\right)^{-}, \text{ at } X_2 = 0 \tag{S32}$$

where

$$\left(\overline{U}_1, \overline{U}_2\right)^{+} = \left(-c_1 - c_2 r^{-1} + c_3 + c_4 r^{-1}, c_1 + c_2 + c_3 + c_4\right) \tag{S33}$$

$$\left(\overline{U}_1, \overline{U}_2\right)^{-} = \left(-c_1 - c_2 r_s^{-1} + c_3 + c_4 r_s^{-1}, c_1 + c_2 + c_3 + c_4\right) \tag{S34}$$

By combining **Supplementary Eqs. S27**, **S29** and S**32**, we obtain the following equation

$$\mathbf{D}\begin{bmatrix} c_1 \\ c_2 \\ c_3 \\ c_4 \end{bmatrix} = \mathbf{0} \tag{S35}$$

The existence of roots requires the determinant of the coefficient matrix $\mathbf{D}$ in **Supplementary Eq. S35** to be zero, *i.e.,* $\det(\mathbf{D})=0$. For wrinkling instability induced by mismatch strain ε_M, the pre-stretch ratio λ_p should be set as a variable as $\lambda_p = 1/\lambda_{1f}$. The resultant critical compressive strain $\varepsilon = 1-\lambda_{1f}$ should be minimized over kH_f. The calculated critical mismatch strain is plotted in **Supplementary Fig. S2C** as a function of μ_f/μ_s.

Parameter estimation of growing/swelling film-substrate systems in reported studies

In **Table 1**, two types of parameters are estimated from the materials used in the films and substrates and marked in gray boxes: $\Gamma/(\mu_s H_f)>10^3$ indicates the film-substrate adhesion is strong enough to avoid delamination between them; $\mu_f/\mu_s<10^{-3}$ indicates the modulus of the film is much smaller than that of the substrate. Other parameters are estimated from the data given in the corresponding references and discussed as follow. In reference 5[5], the instability pattern is identified as fold (shown in Fig. 4C in reference 5[5], similar pattern in reference 6[6]). The compression ratio in the film (Endoderm) is g_{fx} =1-0.7, and the compression ratio in the substrate (Mesenchyme) is g_{sx} =0.6-0.5; therefore, the mismatch strain is calculated as $\varepsilon_M = 1-g_{sx}/g_{fx}$ =0.29-0.4. The film-substrate modulus ratio is μ_f/μ_s =1.5-15. In reference 7[7], the analysis is focused on the wrinkling initiation on the brain cortex. The mismatch strain (ε_M =0.05-0.18) is estimated by considering the change of film area, and modulus ratio is larger than 100 and is estimated to be 100-300. In reference 8[8], the differential growth of mucosal region on a softer tissue induces wrinkles in the inner surface of airways. The mismatch strain (ε_M =0.1-0.15) and modulus ratio (μ_f/μ_s =15-50) are given in the paper. Reference 9[9] analyzes wrinkle and period-double on the inner surface of the gut. The mismatch strain is estimated from the growth factors g by using $\varepsilon_M = 1-1/g$, and the modulus ratio (μ_f/μ_s =10-100) is given in the paper. Reference 10[10] is

focused on wrinkling instability of an epithelia cell layer on an elastic stroma. The modulus ratio (μ_f/μ_s ~25) is estimated from the data in the caption of Fig. 1 in reference 10[10]. The mismatch strain is estimated to be 0.05-0.2 from the stability analysis. References 11 and 12[11, 12] demonstrate delamination of the epithelial monolayers on the underlying tissues. The mismatch strain is calculated by using $\varepsilon_M = \varepsilon/(1+\varepsilon)$, where ε is the applied strain in the experiment (11%, 22% and 28%). The shear modulus of the epithelial cell is estimated as 10^4-10^5 Pa [10], and the thickness the epithelial cell layer is estimated as 10 μm. The shear modulus of the silicone substrate is estimated to be in a reasonable range of 10^3-10^5 Pa, and the adhesion energy is estimated as ~10^{-2} J/m^2 ; therefore, the modulus ratio is 1-100 and the normalized adhesion energy $\Gamma/(\mu_s H_f)$ is around 10^{-3}-1. Reference 13[13] investigates the wrinkling instability of blood cell surface. The modulus ratio is directly extracted from the context, and the mismatch strain is estimated by using $\varepsilon_M = \varepsilon/(1+\varepsilon)$, where ε is the growth strain. Reference 14[14] studies the delaminated-buckles on growing biofilm on a culture gel. The shear modulus of the biofilm is μ_f =2.7-16.5 kPa, and the shear modulus of the agar gel substrate is estimated as μ_s =1-100 kPa; so the modulus ratio is around μ_f/μ_s =0.3-16. The thickness of the biofilm is H_f =0.5-1 mm; the adhesion energy density is estimated as $\Gamma = 0.01-0.1 J/m^2$ [15]; the normalized adhesion energy is thus calculated as $\Gamma/(\mu_s H_f) \approx 10^{-3}$ -0.2. The mismatch strain 0-0.4 is estimated from the cross-section images of the buckled biofilm. The delaminated buckle pattern of the biofilm in reference 14[14] is very similar to the patterns in references 16 and 17[16, 17]. References 18 and 19[18, 19] are focused on wrinkling instability on fruits and plants. The mismatch strain is directly extracted from the relative magnitude of shrinkage, and modulus ratio is from the context. When the mismatch strain is larger than 0.3, the wrinkle mode transits into a period-double-like mode. A similar wrinkling instability of a drying apple is analyzed in reference 20[20]. References 21-24[21-24] analyze creasing instability in a swelling hydrogel on a rigid substrate. The critical mismatch strain for the creasing instability is observed as 0.32-0.38 [22, 23]. In reference 25[25], crease,

wrinkle and fold have been observed in bilayer swelling hydrogel system. If $\mu_f/\mu_s<1$, creases emerge on the outer ring of the hydrogel; however, if $\mu_f/\mu_s>1$, the system first wrinkles and then transits into the fold mode. The corresponding shear modulus and mismatch strain are directly extracted from the context of reference 25[25]. The wrinkle to fold transition has also been observed in reference 26[26], and the experimental data are directed extracted from its context. Reference 27[27] is focused on creasing to delaminated-buckling in a swollen silicone film (Sylgard, base:cross-linker=10:0.4) bonded on a rigid substrate. The swelling ratio of Sylgard in toluene by weight is 380%; the density of toluene and Sylgard are 866.90 kg/m³ and 965.00 kg/m³, respectively; the swelling ratio by volume is thus estimated as 412%; the maximum mismatch strain is then calculated as $\varepsilon_M \approx 0.51$. The film thickness is $H_f \approx 20\mu$m, and its shear modulus is μ_f=18 kPa. The shear modulus of acrylic substrate is ~100 MPa. The film-substrate adhesion is estimated as 0.1-10 J/m^2, so the normalized adhesion energy is estimated as $\Gamma/(\mu_s H_f)\approx$ 5×10^{-5}-5×10^{-3}. Reference 28[28] studies wrinkling instability of a swelling UV-ozone treated Sylgard thin film on a normal Sylgard. The mismatch strain is estimated by the swelling ratio. The shear moduli of the UV-ozone treated film and the Sylgard substrate are estimated as ~1 GPa and 100 kPa, respectively; so the modulus ratio is around 10^4.

Supplementary References

1. Cao, Y., Hutchinson, J. W. From wrinkles to creases in elastomers: the instability and imperfection-sensitivity of wrinkling. *Proc. R. Soc. A* **468**, 94-115 (2012).

2. Cao, Y., Hutchinson, J. W. Wrinkling phenomena in neo-Hookean film/substrate bilayers. *J. Appl. Mech.* **79**, 1019 (2012).

3. Hutchinson, J. W. The role of nonlinear substrate elasticity in the wrinkling of thin films. *Phil. Trans. R. Soc. A* **371**, (2013).

4. van der Heijden, A. M. *WT Koiter's elastic stability of solids and structures* (Cambridge University Press Cambridge, 2009).

5. Shyer, A. E.*, et al.* Villification: How the Gut Gets Its Villi. *Science* **342**, 212-218 (2013).

6. Amar, M. B., Jia, F. Anisotropic growth shapes intestinal tissues during embryogenesis. *Proc. Natl. Acad. Sci. U.S.A.* **110**, 10525-10530 (2013).

7. Richman, D. P., Stewart, R. M., Hutchinson, J. W., Caviness Jr, V. S. Mechanical model of brain convolutional development. *Science* **189**, 18-21 (1975).

8. Wiggs, B. R., Hrousis, C. A., Drazen, J. M., Kamm, R. D. On the mechanism of mucosal folding in normal and asthmatic airways. *J. Appl. Physiol.* **83**, 1814-1821 (1997).

9. Wang, Q., Tahir, M., Zhang, L., Zhao, X. Electro-creasing instability in deformed polymers: experiment and theory. *Soft Matter* **7**, 6583-6589 (2011).

10. Hannezo, E., Prost, J., Joanny, J. F. Instabilities of Monolayered Epithelia: Shape and Structure of Villi and Crypts. *Phys. Rev. Lett.* **107**, 078104 (2011).

11. Eisenhoffer, G. T.*, et al.* Crowding induces live cell extrusion to maintain homeostatic cell numbers in epithelia. *Nature* **484**, 546-549 (2012).

12. Marinari, E.*, et al.* Live-cell delamination counterbalances epithelial growth to limit tissue overcrowding. *Nature* **484**, 542-545 (2012).

13. Wang, L., Castro, C. E., Boyce, M. C. Growth strain-induced wrinkled membrane morphology of white blood cells. *Soft Matter* **7**, 11319-11324 (2011).

14. Asally, M.*, et al.* Localized cell death focuses mechanical forces during 3D patterning in a biofilm. *Proc. Natl. Acad. Sci. U.S.A.* **109**, 18891-18896 (2012).

15. Chen, M., Zhang, Z., Bott, T. Direct measurement of the adhesive strength of biofilms in pipes by micromanipulation. *Biotechnol. Tech.* **12**, 875-880 (1998).

16. DePas, W. H.*, et al.* Iron induces bimodal population development by Escherichia coli. *Proc. Natl. Acad. Sci. U.S.A.* **110**, 2629-2634 (2013).

17. Wilking, J. N.*, et al.* Liquid transport facilitated by channels in Bacillus subtilis biofilms. *Proc. Natl. Acad. Sci. U.S.A.* **110**, 848-852 (2012).

18. Li, B., *et al.* Surface wrinkling patterns on a core-shell soft sphere. *Phys. Rev. Lett.* **106**, 234301 (2011).

19. Yin, J., *et al.* Stress-driven buckling patterns in spheroidal core/shell structures. *Proc. Natl. Acad. Sci. U.S.A.* **105**, 19132-19135 (2008).

20. Cerda, E., Mahadevan, L. Geometry and physics of wrinkling. *Phys. Rev. Lett.* **90**, 074302 (2003).

21. Kim, J., Yoon, J., Hayward, R. C. Dynamic display of biomolecular patterns through an elastic creasing instability of stimuli-responsive hydrogels. *Nat. Mater.* **9**, 159-164 (2010).

22. Trujillo, V., Kim, J., Hayward, R. C. Creasing instability of surface-attached hydrogels. *Soft Matter* **4**, 564-569 (2008).

23. Yoon, J., Kim, J., Hayward, R. C. Nucleation, growth, and hysteresis of surface creases on swelled polymer gels. *Soft Matter* **6**, 5807-5816 (2010).

24. Tanaka, T., *et al.* Mechanical instability of gels at the phase transition. *Nature* **325**, 796-798 (1987).

25. Dervaux, J., Couder, Y., Guedeau-Boudeville, M.-A., Amar, M. B. Shape transition in artificial tumors: from smooth buckles to singular creases. *Phys. Rev. Lett.* **107**, 018103 (2011).

26. Sultan, E., Boudaoud, A. The Buckling of a Swollen Thin Gel Layer Bound to a Compliant Substrate. *J. Appl. Mech.* **75**, 051002-051002 (2008).

27. Velankar, S. S., Lai, V., Vaia, R. A. Swelling-Induced Delamination Causes Folding of Surface-Tethered Polymer Gels. *ACS Appl. Mater. Interfaces* **4**, 24-29 (2012).

28. Breid, D., Crosby, A. J. Effect of stress state on wrinkle morphology. *Soft Matter* **7**, 4490-4496 (2011).

29. Jiang, H., *et al.* Finite deformation mechanics in buckled thin films on compliant supports. *Proceedings of the National Academy of Sciences* **104**, 15607-15612 (2007).

30. Khang, D. Y., Jiang, H., Huang, Y., Rogers, J. A. A stretchable form of single-crystal silicon for high-performance electronics on rubber substrates. *Science* **311**, 208-212 (2006).